Report

Current Biology

EB1 Directly Regulates APC-Mediated Actin Nucleation

Graphical Abstract

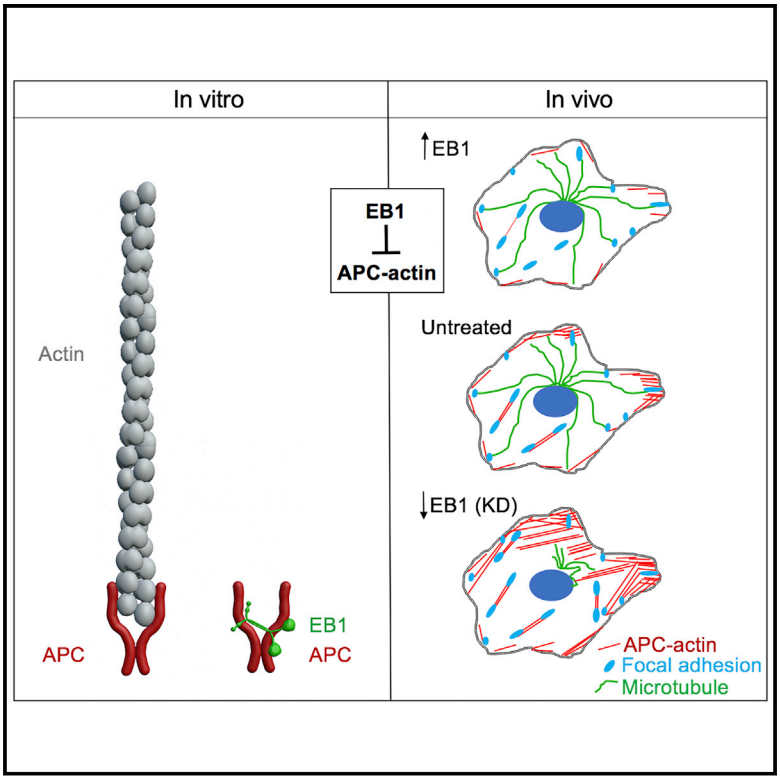

Authors

Maria Angeles Juanes, Colby P. Fees, Gregory J. Hoeprich, Richa Jaiswal, Bruce L. Goode

Correspondence

m.juanes@tees.ac.uk (M.A.J.), goode@brandeis.edu (B.L.G.)

In Brief

Juanes et al. show that EB1, a key regulator of microtubule dynamics, directly inhibits APC-mediated actin assembly *in vitro* and governs APC-dependent cellular F-actin levels and directed cell migration. These results suggest that EB1 promotes bidirectional cytoskeletal crosstalk by coordinating microtubule and actin dynamics.

Highlights

- EB1 inhibits APC-mediated actin assembly *in vitro* by blocking G-actin recruitment
- EB1 negatively regulates APC-dependent actin assembly in cells
- Altering EB1 levels results in defects in cell migration and focal adhesions
- EB1 regulates cellular actin independent of its direct binding to microtubules

Juanes et al., 2020, Current Biology *30*, 1–10
December 7, 2020
https://doi.org/10.1016/j.cub.2020.08.094

CellPress

Please cite this article in press as: Juanes et al., EB1 Directly Regulates APC-Mediated Actin Nucleation, Current Biology (2020), https://doi.org/10.1016/j.cub.2020.08.094

Current Biology

CellPress
OPEN ACCESS

Report

EB1 Directly Regulates APC-Mediated Actin Nucleation

Maria Angeles Juanes,[1,2,3,*] Colby P. Fees,[1] Gregory J. Hoeprich,[1] Richa Jaiswal,[1] and Bruce L. Goode[1,4,*]
[1]Biology Department, Brandeis University, 415 South Street, Waltham, MA 02454, USA
[2]School of Health and Life Science, Teesside University, Middlesbrough TS1 3BX, UK
[3]National Horizons Centre, Teesside University, 38 John Dixon Lane, Darlington DL1 1HG, UK
[4]Lead Contact
*Correspondence: m.juanes@tees.ac.uk (M.A.J.), goode@brandeis.edu (B.L.G.)
https://doi.org/10.1016/j.cub.2020.08.094

SUMMARY

EB1 was discovered 25 years ago as a binding partner of the tumor suppressor adenomatous polyposis coli (APC) [1]; however, the significance of EB1-APC interactions has remained poorly understood. EB1 functions at the center of a network of microtubule end-tracking proteins (+TIPs) [2–5], and APC binding to EB1 promotes EB1 association with microtubule ends and microtubule stabilization [6, 7]. Whether EB1 interactions govern functions of APC beyond microtubule regulation has not been explored. The C-terminal basic domain of APC (APC-B) directly nucleates actin assembly, and this activity is required *in vivo* for directed cell migration and for maintaining normal levels of F-actin [8–10]. Here, we show that EB1 binds APC-B and inhibits its actin nucleation function by blocking actin monomer recruitment. Consistent with these biochemical observations, knocking down EB1 increases F-actin levels in cells, and this can be rescued by disrupting APC-mediated actin nucleation. Conversely, overexpressing EB1 decreases F-actin levels and impairs directed cell migration without altering microtubule organization and independent of its direct binding interactions with microtubules. Overall, our results define a new function for EB1 in negatively regulating APC-mediated actin assembly. Combining these findings with other recent studies showing that APC interactions regulate EB1-dependent effects on microtubule dynamics [7], we propose that EB1-APC interactions govern bidirectional cytoskeletal crosstalk by coordinating microtubule and actin dynamics.

RESULTS AND DISCUSSION

EB1 Directly Inhibits APC-Mediated Actin Nucleation *In Vitro*

EB1 is a master regulator of the microtubule end-tracking protein (+TIP) interaction network, tracking the growing plus ends of microtubules and recruiting other microtubule-associated proteins (MAPs) to microtubule ends [2–5]. EB1 dimers bind to microtubules using calponin homology (CH) domains and have EEY/F motifs that bind proteins with cytoskeleton-associated protein glycine-rich (CAP-Gly) domains and an end-binding homology (EBH) domain that binds proteins with SxIP motifs (where x is any residue) [11–13] (Figure 1A). More recently, EB1 has been shown to bind LxxPTPh motifs (where x is any residue, and h is any hydrophobic residue) [12] (Figure 1A). Notably, adenomatous polyposis coli (APC) contains two previously described SxIP motifs, one located in its basic domain (APC-B) and one in its flanking C-terminal domain [11, 14] (see asterisks in the schematic in Figure 1B). Mutating both SxIP motifs strongly reduces EB1 recruitment of APC to microtubule plus ends *in vitro* [7]; however, it has remained unclear whether these SxIP mutations disrupt all interactions of EB1 with APC, which we address below.

In previous studies, we showed that APC-B potently nucleates actin assembly *in vitro* by dimerizing and recruiting actin monomers to seed polymerization and that this activity is critical for maintaining normal F-actin levels in cells and for directed cell migration [15, 16]. Here we investigated whether EB1 might influence the actin assembly functions of APC. We first tested the *in vitro* effects of full-length EB1 on the actin nucleation activities of APC-B as well as a longer APC-C construct (Figure 1B) [17–19]. In bulk assays, EB1 inhibited the nucleation activity of 20-nM APC-B and APC-C in a dose-dependent manner (Figure 1C; Figure S1A). EB1 also strongly inhibited the collaborative actin assembly effects of APC and the formin Daam1 (Figure S1B). Total internal reflection fluorescence (TIRF) microscopy was used to directly observe actin filaments and verify EB1 inhibition of APC (Figures 1D and 1E; Video S1). The inhibitory effects of EB1 were more potent on APC-C than APC-B, consistent with the presence of the extra SxIP motif in APC-C, which presumably leads to stronger EB1 binding (see below).

We next asked whether EB1 inhibition of APC-mediated actin nucleation is dependent on the two SxIP motifs required for APC's ability to promote EB1 interactions with microtubules [7]. One of the two SxIP motifs is missing in APC-B; therefore, we targeted the remaining motif (SRLP) in APC-B, changing it to LRDP as in Serre et al. [7]. The resulting mutant, APC-B^{LRDP} (S2537L, L2539D), was substantially less active in nucleating actin assembly compared with wild-type APC-B (Figure S1C). This SRLP motif is located within the actin nucleation sequence

Please cite this article in press as: Juanes et al., EB1 Directly Regulates APC-Mediated Actin Nucleation, Current Biology (2020), https://doi.org/10.1016/j.cub.2020.08.094

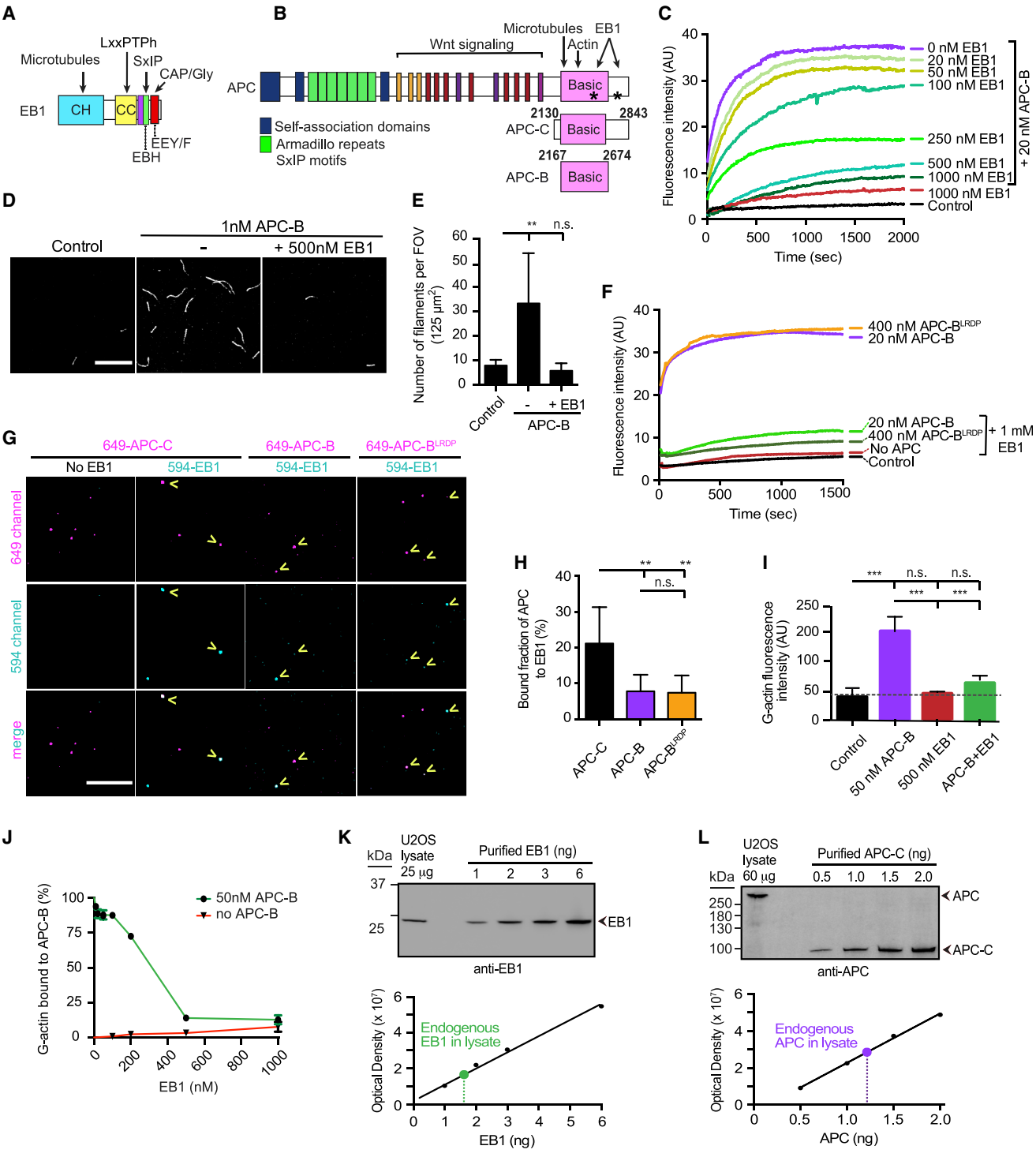

Figure 1. EB1 Directly Inhibits APC-Mediated Actin Nucleation *In Vitro* by Blocking APC-Actin Monomer Interactions

(A) Schematic of EB1 domains and interactions.

(B) Schematic of APC domains and interactions and APC polypeptides used in this study: APC-C (residues 2,130–2,843) and APC-B (residues 2,167–2,674). Asterisks, SxIP motifs.

(C) Bulk actin assembly assays containing 2 μM G-actin (5% pyrene labeled), 5 μM profilin, and other ingredients as indicated.

(D) Representative images captured 1,125 s after initiation of actin assembly in TIRF assays. Reactions contain 1 μM G-actin (10% Oregon green labeled, 0.2% biotin labeled), 5 μM profilin, +/− 1 nM APC-B, +/− 500 nM EB1. Scale bar, 15 μm.

(E) Average number of actin filaments per field of view (FOV) in TIRF assays as in (D). Data are averaged from three independent experiments (two FOVs per experiment). Error bars, SD. One-way ANOVA, Holm-Sidak's multiple comparison test. Statistical differences: **p < 0.01; n.s., not significant.

(legend continued on next page)

Please cite this article in press as: Juanes et al., EB1 Directly Regulates APC-Mediated Actin Nucleation, Current Biology (2020), https://doi.org/10.1016/j.cub.2020.08.094

(ANS2) region of the APC basic domain, which is required for actin nucleation and mediates APC-B dimerization [15, 16]. Thus, mutating SRLP may reduce nucleation activity by weakening dimerization. Using a higher concentration of APC-B^{LRDP} (400 nM), we could reach a nucleation activity equivalent to 20 nM wild-type APC-B and, under these conditions, still observed strong inhibition by EB1 (Figure 1F). These results suggest that the SRLP motif does not mediate key molecular interactions underlying EB1 inhibition of APC-B.

We also used single-molecule imaging to compare binding of labeled EB1 molecules to immobilized fluorescently labeled APC-C, APC-B, and APC-B^{LRDP} molecules, which were tagged with modified O6-alkylguanine-DNA alkyl-transferase (AGT), also known as SNAP-tag (for details regarding specificity and saturation of binding, see STAR Methods). Importantly, SNAP-labeled and unlabeled APC-B had similar effects in actin assembly assays (Figure S1D). Untagged EB1 was directly labeled on a single surface-exposed residue (Cys39) in its CH domain, which did not interfere with its inhibition of APC-mediated actin nucleation (Figure S1E). EB1 interactions with APC-C were stronger than its interactions with APC-B, and EB1 still interacted with APC-B when it carried the APC-B^{LRDP} mutation (Figures 1G and 1H). Together, these results show that the SxIP motifs shown previously to be important for APC's effects on EB1 binding to microtubules [7] are distinct from the interactions that underlie EB1's inhibitory effects on APC-B's actin nucleation activity. Because APC-B does not contain any known EB1-binding elements (CAP-Gly domains or LxxPTPh motifs), its inhibition by EB1 may involve a novel type of molecular interaction that has not yet been characterized.

EB1 Inhibits Actin Monomer Recruitment by APC-B

To better understand how EB1 inhibits APC-mediated actin nucleation, we wanted to find out whether EB1 disrupts APC-B interactions with actin monomers, a requirement for nucleation [18, 19]. We used a binding assay in which APC-B increases the fluorescence of pyrene-G-actin in a concentration-dependent manner [18], reasoning that EB1 binding to APC may reverse APC's effect on pyrene-G-actin fluorescence. Indeed, EB1 inhibited binding of APC-B to G-actin in a concentration-dependent manner, with half-maximal effects at ~300 nM EB1 (Figures 1I and 1J), and EB1 alone had little effect on pyrene-G-actin fluorescence (Figure 1J). These assays were performed in the presence of profilin because profilin was present in our actin assembly assays. Profilin does not interfere with APC binding to G-actin [18]. Together, these observations suggest that EB1 disrupts interactions between APC-B and G-actin to block actin nucleation.

To determine whether the concentrations of EB1 that inhibit APC are in the physiological range, we determined EB1 and APC concentrations in U2OS osteosarcoma cells by quantitative western blotting. The mean and SD from three experiments was 224.90 nM ± 41.96 for EB1 (Figure 1K) and 6.95 nM ± 0.50 for APC in U2OS cells (Figure 1L). These concentrations in U2OS cells are similar to the concentrations of EB1 and APC reported for other cell lines [20, 21]. Thus, the inhibitory effects of EB1 on APC that we observe *in vitro* occur in a physiologically relevant concentration range.

EB1 Regulates APC-Dependent F-actin Levels in Cells

Previously we showed that APC-mediated actin nucleation is required to maintain normal F-actin levels in U2OS cells [15]. Given our *in vitro* observations above, we analyzed the effects of knocking down or overexpressing EB1 on cellular F-actin levels. Western blotting confirmed EB1 silencing, rescue expression, and overexpression (Figure 2A). Cellular F-actin density (intensity per unit cell area) was quantified by Alexa 568-phalloidin staining (representative cell images in Figure 2B; see also Figure S2A; quantification in Figure 2C). There was no significant difference in the mean cell area for any of the compared conditions; thus, a change in average F-actin density corresponds to a change in total F-actin levels. Consistent with our *in vitro* observations, EB1 knockdown led to a substantial increase in F-actin density, and these defects were rescued by expression of RNAi-refractive EB1-GFP at endogenous levels (Figures 2A–2C; Figure S2A). Conversely, EB1-GFP overexpression led to a decrease in F-actin density, similar to cells expressing the nucleation-impaired APC-m4 mutant [15, 16]. Similar results were obtained when cells were fixed by an alternative method that enhances preservation of the actin cytoskeleton (Figures S2B and S2C) [22]. Thus, EB1 negatively regulates F-actin levels in cells. At least some of the effects of EB1 silencing on cellular F-actin levels was due to an increase in stress fibers, as indicated by alpha-actinin immunostaining (Figures S2D and S2E). As

(F) Bulk actin assembly assays containing 2 μM G-actin (5% pyrene labeled), 5 μM profilin, and other ingredients as indicated.
(G) Representative images from single-molecule colocalization assays. 25 pM Biotin-649-labeled SNAP-APC-C, SNAP-APC-B, or SNAP-APC-B^{LRDP}, without or with 500 nM 594-labeled EB1, was incubated and then flowed into the chamber. Yellow arrowheads indicate examples of 594-EB1 molecules colocalizing with surface-anchored Biotin-649-APC molecules. Scale bar, 10 μm.
(H) Analysis of assays as in (G), quantifying the fraction of Biotin-anchored 649-SNAP-APC molecules that showed colocalization of 594-EB1. Data are averaged from six independent experiments for APC-B and seven for APC-C and APC-B^{LRDP}. 10 FOVs were analyzed per condition per experiment (in total, n > 5,000 APC spots per condition). Error bars, SD. Statistical significance was calculated by one-way ANOVA, Holm-Sidak's t test: **p < 0.01, n.s., not significant.
(I) G-actin binding assays in which the fluorescence of 100 nM latrunculin-B (LatB)-bound pyrene-actin monomers increases upon APC-B binding. Reactions contain 5 μM profilin (as in actin assembly assays in C and F) and other ingredients as indicated. Statistical significance was calculated by one-way ANOVA, Holm-Sidak's t test: ***p < 0.001, n.s., not significant.
(J) Concentration-dependent effects of EB1 on APC-B binding to G-actin in assays as in (I).
(K and L) Quantitative western blots used to determine the concentrations of endogenous EB1 and APC proteins in U2OS cells. Each panel shows a representative blot (from three independent trials) probed with anti-EB1 antibodies (K) or anti-APC antibodies (L), comparing the endogenous EB1 or APC signal in the cell lysate lane with known quantities of purified EB1 or APC-C proteins. Standard curves generated from each blot are shown below. The cellular concentrations of EB1 (201, 200, and 273 nM) and APC (7.5, 6.9, and 6.5 nM) were determined from each of the three independent blots (STAR Methods) and then averaged (EB1, 225 nM; APC, 7 nM).
See also Figure S1 and Video S1.

Please cite this article in press as: Juanes et al., EB1 Directly Regulates APC-Mediated Actin Nucleation, Current Biology (2020), https://doi.org/10.1016/j.cub.2020.08.094

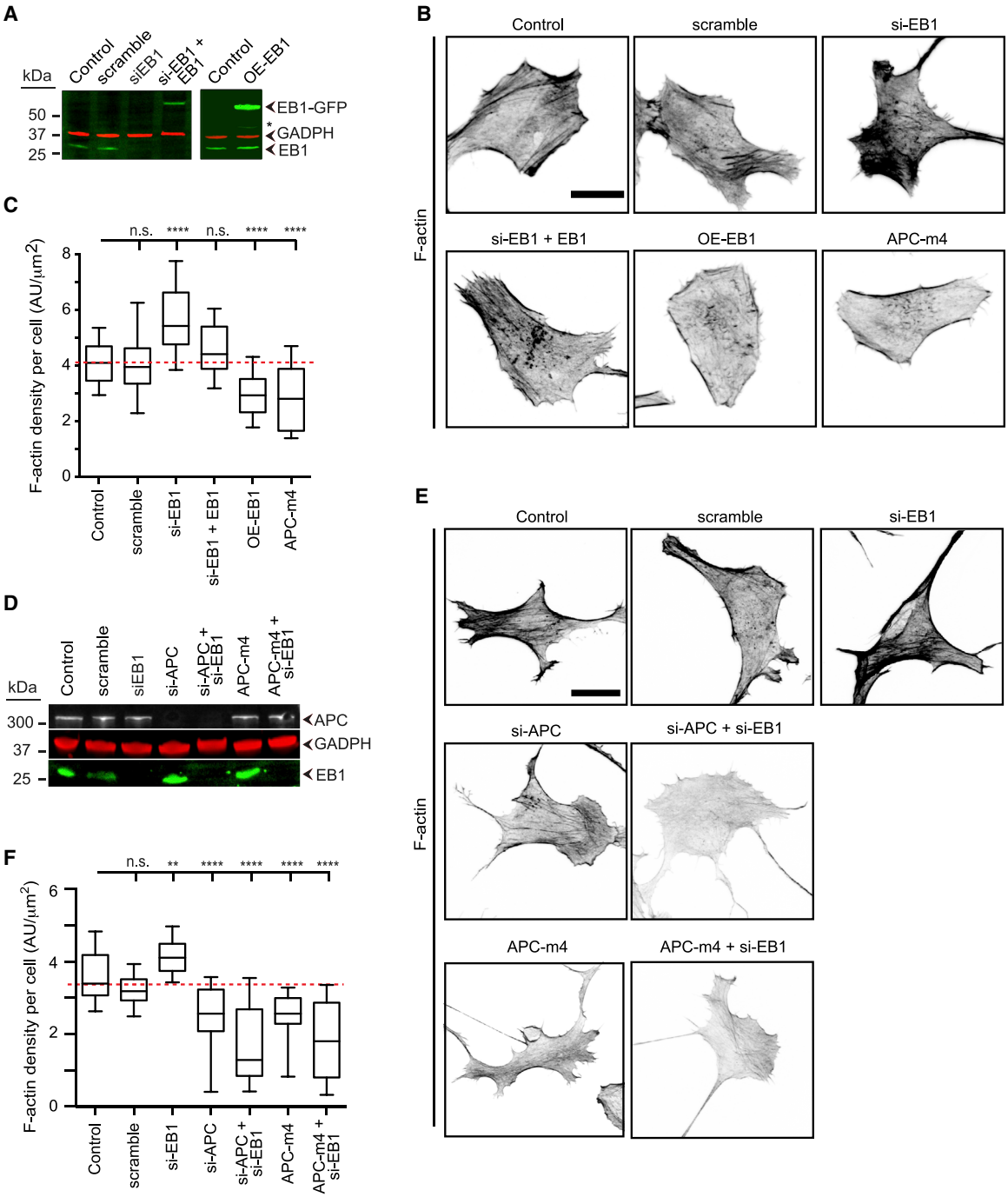

Figure 2. EB1 Regulates APC-Dependent F-actin Levels in Cells

(A) Representative western blots (from three independent blots) showing EB1 and EB1-GFP levels in whole-cell extracts from U2OS cells: untreated WT (Control), mock-treated (scramble), EB1 knockdown (si-EB1; 96% depletion), knockdown and rescue by RNAi-refractive EB1-GFP (99% depletion, 1.4-fold higher level than endogenous EB1), and overexpression of EB1-GFP (OE-EB1; 3.4-fold higher level). Blots were probed with antibodies to EB1 and Glyceraldehyde 3-phosphate dehydrogenase (GADPH, loading control). The asterisk marks an extra band, likely from degradation of GFP-EB1. The expression levels stated above represent the means from three independent experiments.

(B) Representative images of F-actin organization (Alexa 568-phalloidin staining) in cells as in (A) and cells expressing the APC-m4 mutant, which is impaired in actin nucleation. Scale bar, 25 μm.

(C) Quantification of F-actin levels in cells. Box-and-whisker plots represent the mean and 10–90 percentile values for F-actin density (intensity over cell area) per cell, measured from images as in (B). Data are averaged from three independent experiments (left to right: n = 55, 33, 63, 49, and 42 cells). The red dotted line indicates the mean from control cells. Statistical significance was calculated by one-way ANOVA, Holm-Sidak's t test: ****$p < 0.0001$, n.s., not significant.

(legend continued on next page)

Please cite this article in press as: Juanes et al., EB1 Directly Regulates APC-Mediated Actin Nucleation, Current Biology (2020), https://doi.org/10.1016/j.cub.2020.08.094

reported previously [15, 16], APC silencing led to a decrease in stress fiber levels.

To determine whether EB1's effects on F-actin levels in cells are APC-dependent, we wanted to find out whether they could be suppressed by depletion of APC or by expression of APC-m4. Western blotting confirmed APC and EB1 silencing and/or expression of APC-m4 (Figure 2D). Analysis of F-actin density showed that APC silencing or expression of APC-m4 suppressed EB1 knockdown effects (representative cell images in Figure 2E; see also Figure S2F; quantification in Figure 2F). These results support a model in which EB1 negatively regulates APC-mediated actin assembly in cells.

EB1 Regulates F-actin Levels in Cells Independent of Its Direct Binding Interactions with Microtubules and F-actin

We next considered whether the defects on cellular F-actin levels caused by altering EB1 levels might stem from EB1's direct interactions with microtubules and/or F-actin. Therefore, we compared the effects of overexpressing GFP-tagged EB1 wild type ($EB1^{WT}$), $EB1Q^{102E}$ (which disrupts EB1 binding to microtubules), and $EB1^{K89E}$ (which disrupts EB1 binding to microtubules and F-actin) [23, 24]. Overexpression was confirmed by western blotting (Figure 3A). Both EB1 mutants reduced F-actin density in cells, similar to $EB1^{WT}$ (Figures 3B and 3C; Figure S3). Further, overexpression of $EB1^{WT}$, $EB1^{Q102E}$, and $EB1^{K89E}$ did not alter microtubule organization or microtubule levels at the cell periphery (Figures 3B and 3D; Figure S3). Consistent with previous studies [15, 25], APC silencing led to a strong reduction in peripheral microtubule staining whereas APC-m4 expression did not. Thus, even though silencing EB1 alters microtubule organization [25–27], overexpression of EB1 does not, but it reduces F-actin levels. However, these effects on F-actin caused by EB1 overexpression do not depend on its direct interactions with microtubules or F-actin. We propose instead that EB1 regulates APC to control F-actin levels in cells.

EB1 Levels Govern Directed Cell Migration and F-actin Levels at Focal Adhesions

Because the directional migration of MDA-MB-231 breast cancer cells critically depends on APC-mediated actin nucleation [15], we wanted to find out whether increasing or decreasing EB1 levels might alter cell migration. Western blotting verified EB1 silencing and overexpression in MDA-MB-231 cells (Figure 4A). Motility assays were performed on cells migrating toward a chemoattractant gradient (0%–10% fetal bovine serum [FBS]), and the migration paths of more than 971 cells per condition were analyzed using FastTrack AI automated analysis (Video S2; STAR Methods). Rose plots showed that control cells migrated in a polarized manner toward the gradient, whereas cells depleted of EB1 or overexpressing EB1 migrated more randomly (Figure 4B), similar to the reported effects of APC-m4 [15, 16]. Analysis of the migration data showed that altering EB1 levels (up or down) led to a decrease in cell migration velocities, directionality indexes, and Euclidean distances (the shortest distance between start and end points), indicative of random cell migration (Figures 4C–4E). In addition, EB1 depletion or overexpression in U2OS cells caused defects in cell migration in wound healing assays (Figures 4G–4I; Video S3). Analysis of the trajectories of individual cells migrating at the edge of wounds showed that EB1 depletion impaired the speed and directionality of cell movement, whereas EB1 overexpression led to erratic motility with only slightly reduced velocity (Figure 4I). Overexpression of $EB1^{Q102E}$ (defective in microtubule binding) and $EB1^{K89E}$ (defective in microtubule and F-actin binding) led to similar defects in overexpressed $EB1^{WT}$ (Figures 4F–4I; Video S3), demonstrating that the effects of EB1 overexpression on cell migration are independent of its direct binding interactions with microtubules and F-actin. Together, our observations above show that perturbation of normal EB1 levels, up or down, disrupts directional cell migration. Importantly, our data do not rule out the possibility that some of the defects caused by EB1 overexpression are the result of misregulation of its other binding partners. However, the observation that EB1 overexpression causes defects similar to APC-m4 is consistent with a model in which elevated EB1 inhibits APC-mediated actin assembly, which, in turn, disrupts cell motility. On the other hand, cell migration defects caused by EB1 knockdown are likely to also involve loss of EB1 regulatory effects on microtubule dynamics [25–27].

Finally, we asked whether EB1 regulates actin assembly at focal adhesions, given that EB1 localizes to these structures [28–30] and given that focal adhesion turnover depends on APC-mediated actin nucleation [15, 16, 31, 32]. To assess F-actin levels at focal adhesions, U2OS cells were co-stained with Alexa 568-phalloidin and Phospho-Paxillin (P-Pax) (Figure 4J). Overexpression of $EB1^{WT}$, $EB1^{Q102E}$, or $EB1^{K89E}$ significantly reduced F-actin levels at focal adhesions, similar to APC-m4 (Figures 4J and 4K). These results support a role of EB1 in regulating APC-mediated actin assembly to control focal adhesion turnover and, in turn, directed cell migration.

Conclusions

EB1 was first identified 25 years ago as an *in vivo* binding partner of APC [1], and subsequent studies demonstrated that EB1-APC interactions govern microtubule dynamics [6, 7]. However, the potential roles of EB1 in regulating other functions of APC have remained unexplored until now. Our results

(D) Representative western blots (from two independent blots) showing APC and EB1 levels in whole-cell extracts from U2OS cells: untreated WT (control), mock-treated (scramble), EB1 knockdown (si-EB1; 96% depletion), APC knockdown (si-APC; 85% depletion), APC and EB1 double knockdown (si-APC and si-EB1; 91% and 91% respectively), ectopic expression of APC-m4 (78% transfection efficiency), and APC-m4 combined with EB1 knockdown (APC-m4, 80% transfection efficiency; si-EB1, 98% depletion). Blots were probed with antibodies to APC, EB1, and GADPH (loading control).

(E) Representative images of F-actin organization (Alexa 568-phalloidin staining) in cells as in (D). Scale bar, 25 μm.

(F) Quantification of F-actin densities in cells. Box-and-whisker plots represent the mean and 10–90 percentile values for F-actin density (intensity over cell area) per cell, measured from cell images as in (E). Data are averaged from two independent experiments (left to right/up and down: n = 29, 23, 65, 51, 21, 29, and 46 cells). The red dotted line indicates the mean from control cells. Statistical significance was calculated by one-way ANOVA, Holm-Sidak's t test: ****$p < 0.0001$, **$p < 0.01$, n.s., not significant.

See also Figure S2.

Please cite this article in press as: Juanes et al., EB1 Directly Regulates APC-Mediated Actin Nucleation, Current Biology (2020), https://doi.org/10.1016/j.cub.2020.08.094

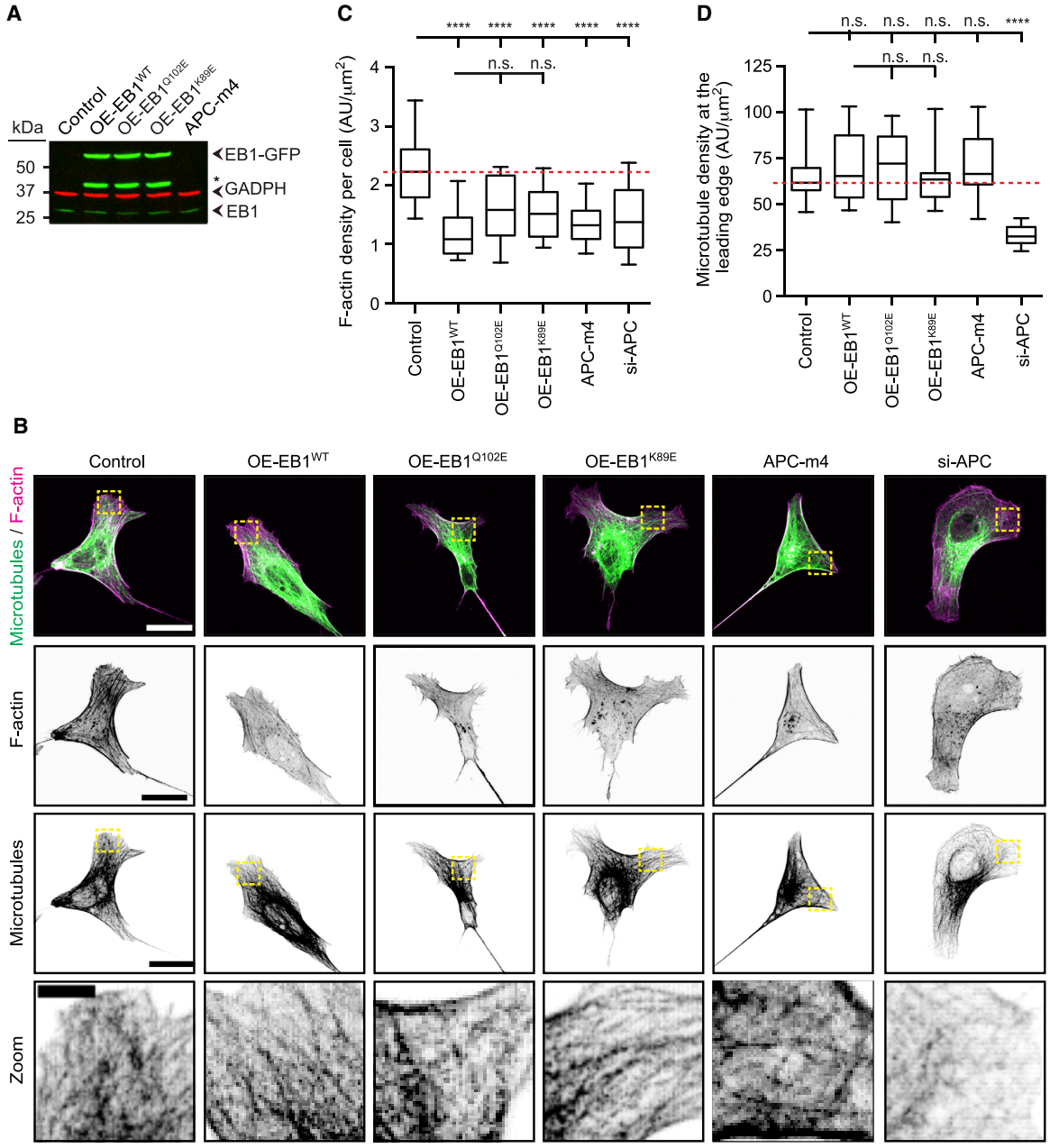

Figure 3. Mutational Dissection of EB1 Effects on Cellular F-actin Levels and Microtubule Organization

(A) Representative western blots (from three independent blots) showing endogenous and overexpressed EB1 levels in U2OS cells: untreated WT (Control), overexpressing GFP-tagged EB1^{WT} (13.4-fold higher than endogenous EB1), overexpressing GFP-tagged EB1^{Q102E} (12-fold higher), overexpressing GFP-tagged EB1^{K89E} (18-fold higher), and expressing APC-m4. The OE levels above are the means from three independent experiments. Transfection efficiencies for all plasmids were 75%–80%.

(B) Representative cell images showing F-actin (Alexa 568-phalloidin staining) and microtubules (tubulin immunostaining) for cells as in (A). Cells depleted of APC (si-APC) were included as an additional control. Scale bar, 25 μm. Boxed regions (yellow) correspond to lower magnified panels (scale bar, 5 μm) and highlight microtubule staining at the leading edge.

(C) Quantification of F-actin levels in cells. Box-and-whisker plots represent the mean and 10–90 percentile values for F-actin density (intensity over cell area) per cell measured from images as in (B) and in Figure S3. Data are averaged from two independent experiments (left to right: n = 31, 21, 20, 21, 20, and 20 cells). The red dotted line indicates the mean from control cells. Statistical significance was calculated by one-way ANOVA, Holm-Sidak's t test: ****$p < 0.0001$. n.s., not significant.

(D) Quantification of microtubule density at the cell periphery (STAR Methods). Box-and-whisker plots represent the mean and 10–90 percentile values for microtubule density at the leading edge from the same cells as in (B) and in Figure S3. Data are averaged from two independent experiments (left to right: n = 21, 21, 20, 21, 20, and 20 cells). The red dotted line indicates the mean from control cells. Statistical significance was calculated by one-way ANOVA, Holm-Sidak's t test: ****$p < 0.0001$, n.s., not significant.

See also Figure S3.

Please cite this article in press as: Juanes et al., EB1 Directly Regulates APC-Mediated Actin Nucleation, Current Biology (2020), https://doi.org/10.1016/j.cub.2020.08.094

CellPress
OPEN ACCESS

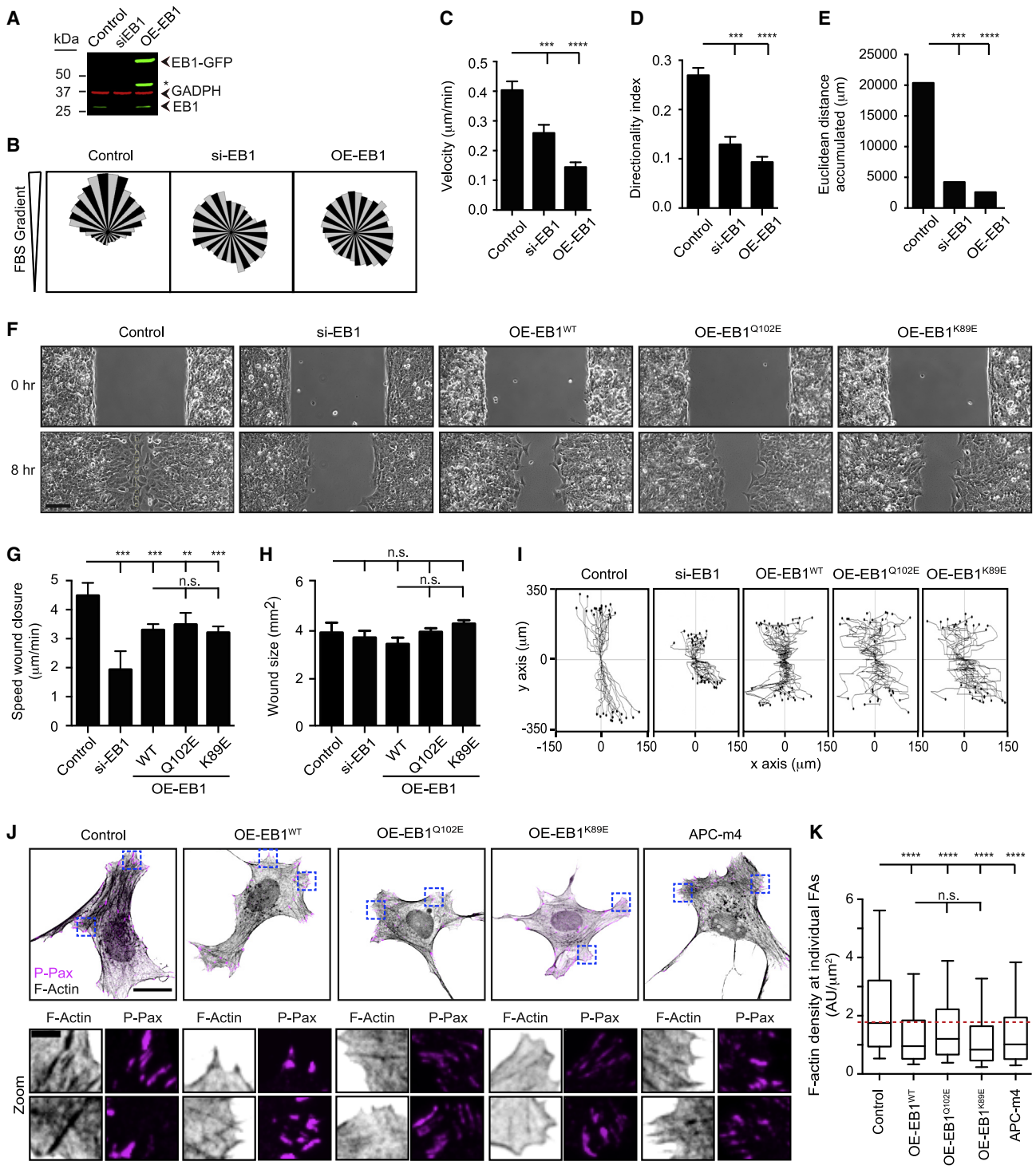

Figure 4. Cellular EB1 Levels Govern Directed Migration and F-actin Density at Focal Adhesions

(A) Representative western blot (from two independent blots) showing EB1 and EB1-GFP levels in whole extracts from MDA-MB-231 cells: untreated (Control), EB1 knockdown (si-EB1; 95% depletion) and overexpressing EB1-GFP (5.8-fold higher than endogenous EB1). Blots were probed with antibodies to EB1 and GADPH (loading control). The asterisk marks an extra band, likely from degradation of GFP-EB1. The expression levels stated above represent the means from two independent experiments.

(B) Rose plots showing cell migration angles toward a gradient of FBS in chemotaxis assays, comparing cells as in (A). Data are pooled from three independent experiments (left to right: n = 1,775, 973, and 1,106 cells).

(legend continued on next page)

Please cite this article in press as: Juanes et al., EB1 Directly Regulates APC-Mediated Actin Nucleation, Current Biology (2020), https://doi.org/10.1016/j.cub.2020.08.094

show that EB1 directly inhibits APC-mediated actin nucleation *in vitro*. Further, EB1 depletion leads to increased F-actin levels in cells, and disrupting APC-mediated actin assembly suppresses this effect. Reciprocally, overexpression of EB1 leads to decreased F-actin levels, consistent with reduced levels of APC-mediated actin nucleation. These overexpression effects are independent of EB1 binding to microtubules, and EB1 inhibition of APC is unaffected by mutations in the SxIP motif of APC-B that mediates EB1-APC microtubule regulatory functions. Thus, EB1 may bind to the basic domain of APC via a non-canonical interaction to block actin assembly. Given that EB1 has many *in vivo* binding partners besides APC, our results do not exclude the possibility that some of its effects upon overexpression or depletion are due to misregulation of other ligands. However, the similarity in phenotypes observed for EB1 overexpression and APC-m4 expression and the ability of APC-m4 expression to partially suppress EB1 overexpression defects suggest that APC-mediated actin assembly is a key target of control for EB1 in cells.

Because EB1-APC interactions are regulated *in vivo* by phosphorylation [6, 7, 33–36] and control not only actin dynamics (our data) but also microtubule dynamics [7], we propose that EB1-APC interactions govern bidirectional microtubule-actin crosstalk by coordinating microtubule and actin dynamics in cells. In the future, it will be important to determine how this is achieved. For instance, when growing microtubule plus ends (enriched in EB1) reach cortical actin structures (e.g., focal adhesions or leading-edge networks), and the microtubules undergo pausing or catastrophe [37–39], they may release EB1 to inhibit APC-mediated actin assembly. Alternatively, growing microtubule ends may locally recruit (or "sponge up") EB1, leading to stimulation of APC-mediated actin assembly. It is our hope that the observations reported here, showing that a direct interaction between these two MAPs (EB1 and APC) controls actin assembly, inspire future investigations into the roles of EB1-APC in cytoskeletal crosstalk in other biological functions and systems.

Finally, does EB1 regulate APC to control cell migration in intact animals? Although truncations in the C terminus of human APC lead to colorectal cancer [40–42], mice lacking the C terminus of APC are viable and fertile and exhibit only minor defects in development [43]. Further, flies lacking the APC gene (APC1) are viable and fertile and show only mild developmental defects [44]. Thus, APC exhibits "phenotypic robustness," which is also seen in many other gene knockouts in mammals and flies, including knockout of the key cytoskeletal regulators CLIP-170 and EB1 [45–49]. This robustness can arise from redundancy with related or unrelated genes or by compensatory changes in expression of factors with related functions. In fact, there is a second APC gene (APC2) in mammals and flies with important cytoskeletal functions [50–53] that could be at least partially redundant with APC/APC1. In addition, there are many other actin nucleation-promoting factors in cells that could compensate for loss of APC in animals. Continued genetic analysis in animals will be required to define the specific pathways and mechanisms that share roles with APC *in vivo*.

STAR★METHODS

Detailed methods are provided in the online version of this paper and include the following:

- KEY RESOURCES TABLE
- RESOURCE AVAILABILITY
  - Lead Contact
  - Materials Availability
  - Data and Code Availability
- EXPERIMENTAL MODEL AND SUBJECT DETAILS
- METHOD DETAILS
  - Plasmid construction
  - Protein purification
  - Bulk assays
  - *In vitro* TIRF microscopy and single molecule binding assays
  - RNAi silencing and plasmid transfections
  - Western blotting
  - Immunostaining of fixed cells
  - Wound healing and chemotaxis assays
- QUANTIFICATION AND STATISTICAL ANALYSIS

SUPPLEMENTAL INFORMATION

Supplemental Information can be found online at https://doi.org/10.1016/j.cub.2020.08.094.

(C–E) Data from (B) were analyzed using FastTrack AI automated analysis to determine migration velocity (C), directionality index (D), and Euclidean distance (E). Shown are the means from three independent experiments. Error bars, SEM. Statistical significance was calculated by one-way ANOVA, Holm-Sidak's t test: ***$p < 0.001$, ****$p < 0.0001$.

(F) Representative images of wound healing assays at 0 and 8 h from U2OS cells: untreated WT (control), mock-treated (scramble), EB1 knockdown (si-EB1), and overexpressing GFP-tagged $EB1^{WT}$, $EB1^{Q102E}$, or $EB1^{K89E}$. Scale bar, 100 μm.

(G) Quantification of wound healing assays as in (F) to compare the speed of wound closure. Data represent the mean from six independent experiments. Error bars, SEM. Statistical significance was calculated by one-way ANOVA, Holm-Sidak's t test: **$p < 0.01$, ***$p < 0.001$, n.s., not significant.

(H) Initial wound sizes (t = 0 h) were not significantly different under all conditions. Data represent the mean from six independent experiments. Error bars, SEM. Statistical significance was calculated by one-way ANOVA, Holm-Sidak's t test: n.s., not significant.

(I) Representative traces of migration paths for individual cells as in (F) at the wound edge; i.e., moving into the wound (n = 35–38 cells per condition). Paths are displayed in radial arrays where the center (x = 0, y = 0) is the starting point of the migration path.

(J) Representative confocal images showing F-actin staining (Alexa-Phalloidin 633) and focal adhesion staining (P-Pax, Phospho-Paxillin Tyr118) in U2OS cells: untreated WT (control); overexpressing GFP-tagged $EB1^{WT}$, $EB1^{Q102E}$, or $EB1^{K89E}$; and expressing APC-m4. Scale bar, 25 μm. Boxed regions (blue) correspond to lower magnified panels (scale bar, 4 μm), highlighting focal adhesions.

(K) Box-and-whisker plots showing F-actin density (fluorescence per unit area) at individual focal adhesions, measured from images as in (J). Graphs show mean and 10–90 percentile values. Data are averaged from two independent experiments (left to right: n = 1,320, 957, 982, 848, and 1,152 focal adhesions). Statistical significance was calculated by one-way ANOVA, Holm-Sidak's t test: ****$p < 0.0001$, n.s., not significant.

See also Videos S2 and S3.

ACKNOWLEDGMENTS

We are grateful to Leon Fan for assistance with protein purification, David W. Drell for help with the automated cell migration tracking analysis, and Jessica L. Henty-Ridilla and Marisa Segal for comments on the manuscript. This work was supported by an NIH R35 award GM134895 (to B.L.G.).

AUTHOR CONTRIBUTIONS

Conceptualization, B.L.G., R.J., M.A.J., and C.P.F.; Methodology and Investigation, B.L.G., R.J., M.A.J., C.P.F., and G.J.H.; Formal Analysis, M.A.J. and C.P.F.; Writing, B.L.G. and M.A.J.; Resources, B.L.G.; Supervision, B.L.G. and M.A.J.; Funding Acquisition, B.L.G.

DECLARATION OF INTERESTS

The authors declare no competing interests.

Received: February 3, 2020
Revised: July 7, 2020
Accepted: August 26, 2020
Published: October 1, 2020

REFERENCES

1. Su, L.K., Burrell, M., Hill, D.E., Gyuris, J., Brent, R., Wiltshire, R., Trent, J., Vogelstein, B., and Kinzler, K.W. (1995). APC binds to the novel protein EB1. Cancer Res. *55*, 2972–2977.
2. Akhmanova, A., and Steinmetz, M.O. (2008). Tracking the ends: a dynamic protein network controls the fate of microtubule tips. Nat. Rev. Mol. Cell Biol. *9*, 309–322.
3. Duellberg, C., Trokter, M., Jha, R., Sen, I., Steinmetz, M.O., and Surrey, T. (2014). Reconstitution of a hierarchical +TIP interaction network controlling microtubule end tracking of dynein. Nat. Cell Biol. *16*, 804–811.
4. Gupta, K.K., Alberico, E.O., Näthke, I.S., and Goodson, H.V. (2014). Promoting microtubule assembly: A hypothesis for the functional significance of the +TIP network. BioEssays *36*, 818–826.
5. Nehlig, A., Molina, A., Rodrigues-Ferreira, S., Honoré, S., and Nahmias, C. (2017). Regulation of end-binding protein EB1 in the control of microtubule dynamics. Cell. Mol. Life Sci. *74*, 2381–2393.
6. Wen, Y., Eng, C.H., Schmoranzer, J., Cabrera-Poch, N., Morris, E.J.S., Chen, M., Wallar, B.J., Alberts, A.S., and Gundersen, G.G. (2004). EB1 and APC bind to mDia to stabilize microtubules downstream of Rho and promote cell migration. Nat. Cell Biol. *6*, 820–830.
7. Serre, L., Stoppin-Mellet, V., and Arnal, I. (2019). Adenomatous Polyposis Coli as a Scaffold for Microtubule End-Binding Proteins. J. Mol. Biol. *431*, 1993–2005.
8. Nelson, S., and Näthke, I.S. (2013). Interactions and functions of the adenomatous polyposis coli (APC) protein at a glance. J. Cell Sci. *126*, 873–877.
9. Akiyama, T., and Kawasaki, Y. (2006). Wnt signalling and the actin cytoskeleton. Oncogene *25*, 7538–7544.
10. McCartney, B.M., and Näthke, I.S. (2008). Cell regulation by the Apc protein Apc as master regulator of epithelia. Curr. Opin. Cell Biol. *20*, 186–193.
11. Honnappa, S., Gouveia, S.M., Weisbrich, A., Damberger, F.F., Bhavesh, N.S., Jawhari, H., Grigoriev, I., van Rijssel, F.J.A., Buey, R.M., Lawera, A., et al. (2009). An EB1-binding motif acts as a microtubule tip localization signal. Cell *138*, 366–376.
12. Kumar, A., Manatschal, C., Rai, A., Grigoriev, I., Degen, M.S., Jaussi, R., Kretzschmar, I., Prota, A.E., Volkmer, R., Kammerer, R.A., et al. (2017). Short linear sequence motif lxxptph targets diverse proteins to growing microtubule ends. Structure *25*, 924–932.e4.
13. Honnappa, S., Okhrimenko, O., Jaussi, R., Jawhari, H., Jelesarov, I., Winkler, F.K., and Steinmetz, M.O. (2006). Key interaction modes of dynamic +TIP networks. Mol. Cell *23*, 663–671.
14. Buey, R.M., Sen, I., Kortt, O., Mohan, R., Gfeller, D., Veprintsev, D., Kretzschmar, I., Scheuermann, J., Neri, D., Zoete, V., et al. (2012). Sequence determinants of a microtubule tip localization signal (MtLS). J. Biol. Chem. *287*, 28227–28242.
15. Juanes, M.A., Bouguenina, H., Eskin, J.A., Jaiswal, R., Badache, A., and Goode, B.L. (2017). Adenomatous polyposis coli nucleates actin assembly to drive cell migration and microtubule-induced focal adhesion turnover. J. Cell Biol. *216*, 2859–2875.
16. Juanes, M.A., Isnardon, D., Badache, A., Brasselet, S., Mavrakis, M., and Goode, B.L. (2019). The role of APC-mediated actin assembly in microtubule capture and focal adhesion turnover. J. Cell Biol. *218*, 3415–3435.
17. Moseley, J.B., Bartolini, F., Okada, K., Wen, Y., Gundersen, G.G., and Goode, B.L. (2007). Regulated binding of adenomatous polyposis coli protein to actin. J. Biol. Chem. *282*, 12661–12668.
18. Okada, K., Bartolini, F., Deaconescu, A.M., Moseley, J.B., Dogic, Z., Grigorieff, N., Gundersen, G.G., and Goode, B.L. (2010). Adenomatous polyposis coli protein nucleates actin assembly and synergizes with the formin mDia1. J. Cell Biol. *189*, 1087–1096.
19. Breitsprecher, D., Jaiswal, R., Bombardier, J.P., Gould, C.J., Gelles, J., and Goode, B.L. (2012). Rocket launcher mechanism of collaborative actin assembly defined by single-molecule imaging. Science *336*, 1164–1168.
20. Alberico, E.O., Lyons, D.F., Murphy, R.J., Philip, J.T., Duan, A.R., Correia, J.J., and Goodson, H.V. (2013). Biochemical evidence that human EB1 does not bind preferentially to the microtubule seam. Cytoskeleton (Hoboken) *70*, 317–327.
21. Tan, C.W., Gardiner, B.S., Hirokawa, Y., Layton, M.J., Smith, D.W., and Burgess, A.W. (2012). Wnt signalling pathway parameters for mammalian cells. PLoS ONE *7*, e31882.
22. DesMarais, V., Eddy, R.J., Sharma, V.P., Stone, O., and Condeelis, J.S. (2019). Optimizing leading edge F-actin labeling using multiple actin probes, fixation methods and imaging modalities. Biotechniques *66*, 113–119.
23. Alberico, E.O., Zhu, Z.C., Wu, Y.O., Gardner, M.K., Kovar, D.R., and Goodson, H.V. (2016). Interactions between the Microtubule Binding Protein EB1 and F-Actin. J. Mol. Biol. *428*, 1304–1314.
24. Maurer, S.P., Fourniol, F.J., Bohner, G., Moores, C.A., and Surrey, T. (2012). EBs recognize a nucleotide-dependent structural cap at growing microtubule ends. Cell *149*, 371–382.
25. Zaoui, K., Benseddik, K., Daou, P., Salaün, D., and Badache, A. (2010). ErbB2 receptor controls microtubule capture by recruiting ACF7 to the plasma membrane of migrating cells. Proc. Natl. Acad. Sci. USA *107*, 18517–18522.
26. Chanez, B., Gonçalves, A., Badache, A., and Verdier-Pinard, P. (2015). Eribulin targets a ch-TOG-dependent directed migration of cancer cells. Oncotarget *6*, 41667–41678.
27. Pustylnik, S., Fiorino, C., Nabavi, N., Zappitelli, T., da Silva, R., Aubin, J.E., and Harrison, R.E. (2013). EB1 levels are elevated in ascorbic Acid (AA)-stimulated osteoblasts and mediate cell-cell adhesion-induced osteoblast differentiation. J. Biol. Chem. *288*, 22096–22110.
28. Zhang, Y., Luo, Y., Lyu, R., Chen, J., Liu, R., Li, D., Liu, M., and Zhou, J. (2016). Proto-Oncogenic Src Phosphorylates EB1 to Regulate the Microtubule-Focal Adhesion Crosstalk and Stimulate Cell Migration. Theranostics *6*, 2129–2140.
29. Yang, C., Wu, J., de Heus, C., Grigoriev, I., Liv, N., Yao, Y., Smal, I., Meijering, E., Klumperman, J., Qi, R.Z., and Akhmanova, A. (2017). EB1 and EB3 regulate microtubule minus end organization and Golgi morphology. J. Cell Biol. *216*, 3179–3198.
30. Su, P., Yin, C., Li, D., Yang, C., Wang, X., Pei, J., Tian, Y., and Qian, A. (2020). MACF1 promotes preosteoblast migration by mediating focal adhesion turnover through EB1. Biol. Open *9*, bio048173.
31. Gardel, M.L., Schneider, I.C., Aratyn-Schaus, Y., and Waterman, C.M. (2010). Mechanical integration of actin and adhesion dynamics in cell migration. Annu. Rev. Cell Dev. Biol. *26*, 315–333.

32. Ridley, A.J., Schwartz, M.A., Burridge, K., Firtel, R.A., Ginsberg, M.H., Borisy, G., Parsons, J.T., and Horwitz, A.R. (2003). Cell migration: integrating signals from front to back. Science *302*, 1704–1709.
33. Morrison, E.E. (2009). The APC-EB1 interaction. Adv. Exp. Med. Biol. *656*, 41–50.
34. Green, R.A., Wollman, R., and Kaplan, K.B. (2005). APC and EB1 function together in mitosis to regulate spindle dynamics and chromosome alignment. Mol. Biol. Cell *16*, 4609–4622.
35. Askham, J.M., Moncur, P., Markham, A.F., and Morrison, E.E. (2000). Regulation and function of the interaction between the APC tumour suppressor protein and EB1. Oncogene *19*, 1950–1958.
36. Morrison, E.E., Wardleworth, B.N., Askham, J.M., Markham, A.F., and Meredith, D.M. (1998). EB1, a protein which interacts with the APC tumour suppressor, is associated with the microtubule cytoskeleton throughout the cell cycle. Oncogene *17*, 3471–3477.
37. Kaverina, I., Rottner, K., and Small, J.V. (1998). Targeting, capture, and stabilization of microtubules at early focal adhesions. J. Cell Biol. *142*, 181–190.
38. Kaverina, I., Krylyshkina, O., and Small, J.V. (1999). Microtubule targeting of substrate contacts promotes their relaxation and dissociation. J. Cell Biol. *146*, 1033–1044.
39. Rodriguez, O.C., Schaefer, A.W., Mandato, C.A., Forscher, P., Bement, W.M., and Waterman-Storer, C.M. (2003). Conserved microtubule-actin interactions in cell movement and morphogenesis. Nat. Cell Biol. *5*, 599–609.
40. Näthke, I.S. (2004). The adenomatous polyposis coli protein: the Achilles heel of the gut epithelium. Annu. Rev. Cell Dev. Biol. *20*, 337–366.
41. Zhang, L., and Shay, J.W. (2017). Multiple roles of APC and its therapeutic implications in colorectal cancer. J. Natl. Cancer Inst. *109*, djw332.
42. Polakis, P. (1997). The adenomatous polyposis coli (APC) tumor suppressor. Biochim. Biophys. Acta *1332*, F127–F147.
43. Smits, R., Kielman, M.F., Breukel, C., Zurcher, C., Neufeld, K., Jagmohan-Changur, S., Hofland, N., van Dijk, J., White, R., Edelmann, W., et al. (1999). Apc1638T: a mouse model delineating critical domains of the adenomatous polyposis coli protein involved in tumorigenesis and development. Genes Dev. *13*, 1309–1321.
44. Ahmed, Y., Hayashi, S., Levine, A., and Wieschaus, E. (1998). Regulation of armadillo by a Drosophila APC inhibits neuronal apoptosis during retinal development. Cell *93*, 1171–1182.
45. Dix, C.I., Soundararajan, H.C., Dzhindzhev, N.S., Begum, F., Suter, B., Ohkura, H., Stephens, E., and Bullock, S.L. (2013). Lissencephaly-1 promotes the recruitment of dynein and dynactin to transported mRNAs. J. Cell Biol. *202*, 479–494.
46. Beaven, R., Dzhindzhev, N.S., Qu, Y., Hahn, I., Dajas-Bailador, F., Ohkura, H., and Prokop, A. (2015). Drosophila CLIP-190 and mammalian CLIP-170 display reduced microtubule plus end association in the nervous system. Mol. Biol. Cell *26*, 1491–1508.
47. Miedema, M. (2007). Cytoplasmic Linker Proteins: Keeping in Shape by Regulating the Cytoskeleton (Erasmus University Rotterdam).
48. Komarova, Y., De Groot, C.O., Grigoriev, I., Gouveia, S.M., Munteanu, E.L., Schober, J.M., Honnappa, S., Buey, R.M., Hoogenraad, C.C., Dogterom, M., et al. (2009). Mammalian end binding proteins control persistent microtubule growth. J. Cell Biol. *184*, 691–706.
49. Komarova, Y., Lansbergen, G., Galjart, N., Grosveld, F., Borisy, G.G., and Akhmanova, A. (2005). EB1 and EB3 control CLIP dissociation from the ends of growing microtubules. Mol. Biol. Cell *16*, 5334–5345.
50. Molinar-Inglis, O., Oliver, S.L., Davison, P., Kunttas, E., and McCartney, B.M. (2018). APC2 associates with the actin cortex through a multi-part mechanism to regulate cortical actin organization and dynamics in the Drosophila ovary. Cytoskeleton *75*, 323–335.
51. Webb, R.L., Zhou, M.-N., and McCartney, B.M. (2009). A novel role for an APC2-Diaphanous complex in regulating actin organization in Drosophila. Development *136*, 1283–1293.
52. Zhou, M.-N., Kunttas-Tatli, E., Zimmerman, S., Zhouzheng, F., and McCartney, B.M. (2011). Cortical localization of APC2 plays a role in actin organization but not in Wnt signaling in Drosophila. J. Cell Sci. *124*, 1589–1600.
53. Kahn, O.I., Schätzle, P., van de Willige, D., Tas, R.P., Lindhout, F.W., Portegies, S., Kapitein, L.C., and Hoogenraad, C.C. (2018). APC2 controls dendrite development by promoting microtubule dynamics. Nat. Commun. *9*, 2773.
54. Spudich, J.A., and Watt, S. (1971). The regulation of rabbit skeletal muscle contraction. I. Biochemical studies of the interaction of the tropomyosin-troponin complex with actin and the proteolytic fragments of myosin. J. Biol. Chem. *246*, 4866–4871.
55. Kuhn, J.R., and Pollard, T.D. (2005). Real-time measurements of actin filament polymerization by total internal reflection fluorescence microscopy. Biophys. J. *88*, 1387–1402.
56. Cooper, J.A., Blum, J.D., and Pollard, T.D. (1984). Acanthamoeba castellanii capping protein: properties, mechanism of action, immunologic cross-reactivity, and localization. J. Cell Biol. *99*, 217–225.
57. Moseley, J.B., Sagot, I., Manning, A.L., Xu, Y., Eck, M.J., Pellman, D., and Goode, B.L. (2004). A conserved mechanism for Bni1- and mDia1-induced actin assembly and dual regulation of Bni1 by Bud6 and profilin. Mol. Biol. Cell *15*, 896–907.
58. Jaiswal, R., Breitsprecher, D., Collins, A., Corrêa, I.R., Jr., Xu, M.-Q., and Goode, B.L. (2013). The formin Daam1 and fascin directly collaborate to promote filopodia formation. Curr. Biol. *23*, 1373–1379.
59. Kovar, D.R., Harris, E.S., Mahaffy, R., Higgs, H.N., and Pollard, T.D. (2006). Control of the assembly of ATP- and ADP-actin by formins and profilin. Cell *124*, 423–435.
60. Amatruda, J.F., and Cooper, J.A. (1992). Purification, characterization, and immunofluorescence localization of Saccharomyces cerevisiae capping protein. J. Cell Biol. *117*, 1067–1076.
61. Soeno, Y., Abe, H., Kimura, S., Maruyama, K., and Obinata, T. (1998). Generation of functional beta-actinin (CapZ) in an E. coli expression system. J. Muscle Res. Cell Motil. *19*, 639–646.
62. Moseley, J.B., and Goode, B.L. (2005). Differential activities and regulation of Saccharomyces cerevisiae formin proteins Bni1 and Bnr1 by Bud6. J. Biol. Chem. *280*, 28023–28033.
63. Smith, B.A., Gelles, J., and Goode, B.L. (2014). Single-molecule studies of actin assembly and disassembly factors. Methods Enzymol. *540*, 95–117.

Please cite this article in press as: Juanes et al., EB1 Directly Regulates APC-Mediated Actin Nucleation, Current Biology (2020), https://doi.org/10.1016/j.cub.2020.08.094

STAR★METHODS

KEY RESOURCES TABLE

REAGENT or RESOURCE	SOURCE	IDENTIFIER
Antibodies		
Rabbit anti-APC	Abcam	Cat# ab154906; RRID:AB_2861396
Mouse anti-EB1	BD Bioscience	Cat# 610534; RRID:AB_397891
Rabbit/human anti-GADPH	Abcam	Cat# ab9485; RRID:AB_307275
Rabbit anti-phospho-Paxillin (Tyr −118)	ECM Biosciences	Cat# PP4501; RRID:AB_2861397
Mouse BM75.2 alpha-actinin	Sigma-Aldrich	Cat# A5044; RRID:AB_476737
Mouse alpha-tubulin antibody	Santa Cruz Biotechnology	Cat# sc-32292; RRID:AB_2110259
Goat anti-mouse AlexaFluor-488	Thermo Fisher Scientific	Cat# A32723; RRID:AB_2633275
Goat anti-rabbit AlexaFluor-555	Thermo Fisher Scientific	Cat# A-21428; RRID:AB_2535849
Goat anti-mouse AlexaFluor-633	Thermo Fisher Scientific	Cat# A-21050; RRID:AB_2535718
Donkey anti-rabbit IRDye 680RD	LI-COR Biosciences	Cat# 926-68073; RRID:AB_10954442
Goat anti-mouse IRDye 680RD	LI-COR Biosciences	Cat# 926-68070; RRID:AB_10956588
Donkey anti-rabbit IRDye 800RD	LI-COR Biosciences	Cat# 926-32213; RRID:AB_621848
Bacterial and Virus Strains		
XL Blue competent cells	Agilent	Cat# 200249
Chemicals, Peptides, and Recombinant Proteins		
Alexa Fluor 594 C5 Maleimide	Thermo Fisher Scientific	Cat# A10256
Turbo Labeling Kit, Cy5 dye	Thermo Fisher Scientific	Cat# KIT0610
EB1	[21]	Bruce Goode-US
594-EB1	This paper	Bruce Goode-US
APC-B	[19]	Bruce Goode-US
SNAP-APC-B	This paper	Bruce Goode-US
APC-C	[19]	Bruce Goode-US
SNAP-APC-C	[19]	Bruce Goode-US
APC-B-LRDP	This paper	Bruce Goode-US
SNAP-APC-B-LRDP	This paper	Bruce Goode-US
Daam1	[19]	Bruce Goode-US
Profilin	[19]	Bruce Goode-US
CapZ	[19]	Bruce Goode-US
AlexaFluor-568-Phalloidin	Invitrogen-Thermo Fisher Scientific	Cat# A12380
AlexaFluor-633-Phalloidin	Invitrogen-Thermo Fisher Scientific	Cat# A22284
200 mM L-glutamine	Thermo Fisher Scientific	Cat# 25030-081
DMEM- Dulbecco's Modified Eagle Medium	Thermo Fisher Scientific	Cat# 11995-073
UltraCulture serum-free medium	Lonza	Cat# 12-725F
FBS – Fetal bovine serum	Sigma-Aldrich	Cat# F9423
Lipofectamine 3000	Thermo Fisher Scientific	Cat# L3000-015
Lipofectamine RNAiMAX	Thermo Fisher Scientific	Cat# 13778075
Opti-MEM reduced serum media	Thermo Fisher Scientific	Cat# 11058021
Collagen I	Corning	Cat# 354236
Glutaraldehyde, EM Grade 25%	Polysciences	Cat# 01909-10
Formaldehyde 16% - methanol free	Thermo Scientific	Cat# 28908

(*Continued on next page*)

Please cite this article in press as: Juanes et al., EB1 Directly Regulates APC-Mediated Actin Nucleation, Current Biology (2020), https://doi.org/10.1016/j.cub.2020.08.094

Continued

REAGENT or RESOURCE	SOURCE	IDENTIFIER
Experimental Models: Cell Lines		
Human osteosarcoma cells: U2OS	ATCC	Cat# HTB-96; RRID:CVCL_0042
Human breast cancer cells: MDA-MB-231	ATCC	Cat# HTB-26; RRID:CVCL_0062
Oligonucleotides		
siRNA targeting sequence against the human EB1: 5′- UUAAAUACUCUUA AGGCAUUU-3′ sense and 5′- AAAUGCCUUAAG AGUAUUUAA-3′ antisense	Integrated DNA Technologies	Custom oligos
siRNA targeting sequence against the human APC: 5′-GGAUCUGUAUC AAGCCGUUTT-3′ sense and 5′- AACGGCUUGA UACAGAUCCTT-3′ antisense	Thermofisher Scientific	Cat# 4390824
Stealth siRNA-control 'scramble' oligos: 5′- CAGUCGCGUU UGCGACUGG-3′	Invitrogen	Cat# 12935-200
Recombinant DNA		
Plasmid: APC-m4	[19]	Bruce Goode-US
Plasmid: EB1-GFP	Addgene	RRID:Addgene_39299
Plasmid: EB1-Q102E-GFP	This paper	Bruce Goode-US
Plasmid: EB1-K89E-GFP	This paper	Bruce Goode-US
Software and Algorithms		
NIS Elements software - version 4.20	Nikon Instruments	https://www.nikoninstruments.com/Products/Software, RRID:SCR_014329
FastTrack AI automated analysis system - Chemotaxis	MetaVi Labs / Ibidi	https://www.metavilabs.com/sites/default/files/help_center/chemotaxis.html, Cat#32200-3
Wound Healing Automated Cellular Analysis System analysis	MetaVi Labs /Ibidi	https://www.metavilabs.com/sites/default/files/help_center/wound_healing.html, Cat# 32000-250
Chemotaxis and Migration Tool version 2.0 software	Ibidi	https://ibidi.com/chemotaxis-analysis/171-chemotaxis-and-migration-tool.html
GraphPad Prism 6.0c	GraphPad Software	RRID: SCR_002798
Adobe Illustrator CS6	Adobe Illustrator (Adobe Systems)	http://www.adobe.com/products/illustrator.html, RRID:SCR_010279
Imaging Lab version 6.0.0 software	Image Lab Software (Biorad)	http://www.bio-rad.com/en-us/sku/1709690-image-lab-software, RRID:SCR_014210
MATLAB R2019a	MATLAB	http://www.mathworks.com/products/matlab/, RRID:SCR_001622
Fiji / ImageJ	NIH – public domain	http://fiji.sc, RRID:SCR_002285
Other		
AquaMount mounting media	Thermo Fisher Scientific	Cat# 14-390-5
Circular Round cover glasses 0.15 mm	Thermo Fischer Scientific	Cat# 12-545-80
μ−Slide chemotaxis collagen IV	Ibidi	Cat# 80322
Culture-Inserts 2 well	Ibidi	Cat# 81176
Ni-NTA-agarose beads	QIAGEN	Cat# 30230
GSTrap column	GE Healthcare	Cat# 45000281
Centricon spin concentrators	Milipore	Cat# UFC800324
G-25 desalting columns (PD-10)	GE Healthcare	Cat# 17085101

Please cite this article in press as: Juanes et al., EB1 Directly Regulates APC-Mediated Actin Nucleation, Current Biology (2020), https://doi.org/10.1016/j.cub.2020.08.094

CellPress
OPEN ACCESS

RESOURCE AVAILABILITY

Lead Contact

Requests for further information and reagents should be directed to and will be fulfilled by the Lead Contact, Bruce Goode (goode@brandeis.edu).

Materials Availability

This study generated new plasmids for purifying proteins, which will be made available upon request to the Lead Contact Bruce Goode.

Data and Code Availability

The processed image data and the original MATLAB code for this article have been deposited to Zenodo: https://zenodo.org/record/4019683#.X2ktiC2ZOgQ: In addition, all of the raw (original and unprocessed) data have been uploaded to a Google Drive and will be made available upon request to the lead contact (Bruce Goode).

EXPERIMENTAL MODEL AND SUBJECT DETAILS

Purified proteins are as described in Method Details. Human osteosarcoma (U2OS, HTB96) and human breast cancer (MDA-MB-231, HTB-26) cell lines were obtained directly from ATCC (American Type Culture Collection; Manassas, VA, USA), where their identities were authenticated by short tandem repeat DNA profiling and they were tested for mycoplasma contamination. Cell lines were used for a maximum of 25 passages. All cells were grown in DMEM (GIBCO, Life technologies, Grand Island, NY, USA) supplemented with 200 mM L-glutamine (Thermo Fisher Scientific, Waltham, MA), 10% fetal bovine serum (FBS; Sigma-Aldrich, St. Louis, MO), and 50 units/ml Penicillin and 50 μg/ml streptomycin (GIBCO, Thermofisher), at 37°C and 5% CO2.

METHOD DETAILS

Plasmid construction

A plasmid (pBG2404) for *E. coli* expression and purification of SNAP-APC-B was constructed by isolating the coding sequence of the APC-Basic domain (residues 2167-2674) from pBG721 (pGEX-6p harboring APC-B) [17] using EcoRI and NotI, and subcloning this DNA fragment into the same sites in pGEX-6p. Site-directed mutagenesis was used to introduce the two point mutations in APC-B^{LRDP} into the same plasmid with these oligos: forward 5′-TCT GAA AGT CCT CTG AGA GAT CCA ATC AAT AGG-3′ and reverse 5′- CCT ATT GAT TGG ATC TCT CAG AGG ACT TTC AGA-3′ (underlined nucleotides deviate from the wild-type sequence). Site-directed mutagenesis also was used to generate EB1 mutants Q102E and K89E, with the following oligos: Q102E, forward 5′-GGA AAG TTT GAG GAC AAT TTT GAA TTC GTT CAG-3′ and reverse 5′-CTG AAC GAA TTC AAA ATT GTC CTC AAA CTT TCC-3′; K89E, forward 5′-ATG GGT GTT GAC GAA ATA ATT CCT GTG GAC-3′ and reverse 5′-GTC CAC AGG AAT TAT TTC GTC AAC ACC CAT-3′ (underlined nucleotides deviate from wild-type sequence).

Protein purification

Rabbit muscle actin (RMA) was purified from acetone powder and Cys-374-labeled with Oregon Green (OG) as described [54, 55]. Actin was partially extracted from skeletal muscle tissue and stored as 'acetone powder' at −80°C. Acetone powder was pulverized using a coffee grinder and liquid N2, resuspended in G-buffer, and cleared by centrifugation at 50,000 x g. The actin was polymerized overnight at 4°C by addition of 50 mM NaCl and 2 mM MgCl2. Then 0.6 M NaCl was added to F-actin to dissociate actin binding proteins, and the F-actin was pelleted by centrifugation at 361,000 x g for 2.5 hr. F-actin pellets were resuspended in G-buffer, dounce-homogenized, and dialyzed three times against G-buffer for 2-3 days. For use in bulk actin assembly assays, RMA was fluorescently labeled with N-(1-pyrenyl) iodoacetamide on cysteine 374 [56]. RMA prepared as above excluding the gel-filtration step was dialyzed against pyrene buffer (25 mM Tris-HCl pH 7.5, 100 mM KCl, 0.02% NaN3, 0.3 mM ATP, and 2 mM MgSO4) for 3-4 hr, and then diluted with pyrene buffer to 1 mg/mL (23.8 μM). A 7-fold molar excess of pyrenyl-iodoacetamide was added, and the actin solution was incubated overnight at 4°C, then aggregates were cleared by low-speed centrifugation. The supernatant (containing F-actin) was centrifuged for 3 hr at 4°C at 264,000 x g in a Ti70 rotor (Beckman Coulter Inc.; Brea, CA) to pellet F-actin. F-actin pellets were homogenized by douncing, dialyzed against G-buffer for 1-2 days, and gel-filtered on a 16/60 S200 column as above. Peak fractions were pooled, aliquoted, snap-frozen, and stored at −80°C until use.

For TIRF microscopy assays, actin was polymerized and labeled overnight at 4°C using a 12 molar excess of oregon green (OG)-iodoacetamide (Thermo Fisher Scientific, Waltham, MA) in labeling buffer (25 mM imidazole pH 7.5, 100 mM KCl, 0.15 mM NaATP, and 2 mM MgCl2). Actin was polymerized and labeled overnight at 4°C by addition of a 12 molar excess of OG-iodoacetamide (Thermo Fisher Scientific, Waltham, MA) in labeling buffer (25 mM imidazole pH 7.5, 100 mM KCl, 0.15 mM NaATP, and 2 mM MgCl2). Labeled actin was pelleted at 100,000 x g for 3 hr at 4°C, resuspended, and dounced in G-buffer, then dialyzed against G-buffer as above. Labeled G-actin was clarified at 264,000 x g for 30 min, and gel filtered using a HiPrep S200 (16/60) column equilibrated in G-buffer. Peak fractions containing OG-RMA were dialyzed against G-buffer with 50% glycerol and stored at −20°C (where it remains stable for months). Every 1-2 weeks, an aliquot of OG-RMA stored at −20°C was dialyzed against fresh G-buffer and

Please cite this article in press as: Juanes et al., EB1 Directly Regulates APC-Mediated Actin Nucleation, Current Biology (2020), https://doi.org/10.1016/j.cub.2020.08.094

clarified by centrifugation at 353,000 x g for 30 min. Actin concentration was determined by absorbance using a Ɛ290 of 26,600 M-1cm-1. Labeling percentage was calculated using the dye Ɛ493 of 77,800 M-1cm-1 with a correction factor (*cf.*) of 0.16991 (Equation 1).

$$[Actin] = \frac{A_{290} - (A_{493} * cf)}{\varepsilon_{290}} \quad \text{Equation 1}$$

6His-C-Daam1 (FH1-FH2-C) was expressed in *S. cerevisiae* strain BJ2168 from a high copy (2 micron) plasmid under control of a galactose-inducible promoter [57]. For each preparation, 2L of yeast cells were grown in synthetic medium lacking uracil and 2% raffinose to OD600 = 0.8, then expression was induced by addition of galactose (2% final), and cells were grown for another 8-12 hr at 30°C. Cells were washed in H2O, frozen in liquid N2, and lysed by mechanical disruption using a coffee grinder and liquid N2. The resulting frozen yeast powder was stored at −80°C until use. C-Daam1 was then purified as described [57, 58]. Briefly, 10 g of frozen yeast powder was resuspended in buffer A [30 mM Imidazole pH 8.0, 0.5 mM DTT, 2XPBS (40 mM sodium phosphate buffer, 200 mM NaCl, pH 7.4)] with 150mM NaCl, 1% NP-40, standard protease inhibitors and 2 mM phenylmethylsulfonyl fluoride (PMSF) until all of the clumps were dissolved, and then cleared by ultracentrifugation at 300,000 x g for 20 min at 4°C in a TLA100.3 rotor (Beckman Coulter Inc.). The supernatant was incubated with 500 μL Ni-NTA-agarose beads (QIAGEN, Valencia, CA) for 2 hr at 4°C, and then beads were washed three times with buffer A containing 350 mM NaCl, followed by three washes with buffer A. Protein was eluted from the beads with buffer A supplemented with 350 mM imidazole (pH 8.0) and 0.5 mM DTT, and purified further on a Superose 6 gel filtration column (GE Healthcare) equilibrated in buffer HEKG5D [20 mM HEPES pH 7.5, 1 mM EDTA, 50 mM KCl, 5% (v/v) glycerol, 1 mM DTT]. Peak fractions were pooled, concentrated, aliquoted, snap frozen, and stored at −80°C.

Human profilin was purified as described [59]. Briefly, a plasmid expressing human profilin [59] was transformed into BL21(DE3) *E. coli* cells, which were then grown to OD600 = 0.5 in Terrific Broth plus antibiotics. Protein expression was induced for 3 hr at 37°C with 0.4 mM IPTG. Cells were harvested by centrifugation and stored at −80°C. Cell pellets were resuspended in lysis buffer (50 mM Tris pH 8.0, DNase, lysozyme and complete protease inhibitors), kept on ice for 20 min, then lysed by sonication (four pulses of 30 s). Lysates were cleared for 30 min at 14,000 rpm, and the supernatant was loaded on a QFF column (GE Healthcare) equilibrated in 20mM Tris pH 8.0 and 50 mM NaCl, and eluted with a salt gradient (0-1 M NaCl). Peak fractions were pooled, concentrated and purified further on a Superdex 75 column (GE Healthcare) equilibrated with in 20 mM Tris pH 8.0 and 50 mM NaCl. Peak fractions were pooled, concentrated, aliquoted, snap frozen, and stored at −80°C.

Human CapZ was purified as described [60]. Briefly, a plasmid expressing human CapZ [61] was transformed into BL21(DE3) pLysS *E. coli* cells, and cells were grown to OD600 = 0.8 in LB plus antibiotics. Protein expression was induced for 3 hr at 37°C with 0.4 mM IPTG. Cells were harvested by centrifugation and stored at −80°C. Cell pellets were resuspended in lysis buffer (20 mM Tris-Cl pH 8.0, 1mM EDTA, 0.2% Triton X-100, lysozyme and complete protease inhibitors), kept on ice for 30 min, and then lysed by sonication (four pulses of 30 s). Lysates were cleared for 30 min at 14,000 rpm at 4°C, and the supernatant was collected and loaded on a QFF column (GE Healthcare) equilibrated in 20 mM Tris pH 8.0 and 50 mM NaCl and eluted with a salt gradient (0-1 M NaCl, 20 mM Tris pH 8.0). Peak fractions were pooled, concentrated and further fractionated on a Superdex 75 column (GE Healthcare) equilibrated with in 20 mM Tris pH 8.0 and 50 mM NaCl. Peak fractions were pooled, loaded on a monoQ column equilibrated in 20 mM HEPES pH 6.8 and 1 mM EDTA, and eluted with a salt gradient (0-500 mM KCl). Peak fractions were pooled, dialyzed overnight into HEK buffer (20 mM HEPES pH 7.5, 1 mM EDTA, and 50 mM KCl), snap frozen in aliquots, and stored at −80°C.

APC-B, APC-C, SNAP-APC-B, and SNAP-APC-C proteins were purified essentially as described [15] with minor modifications, as follows. Briefly, plasmids expressing APC constructs were transformed into *E. coli* BL21(DE3) pLysS cells, and cells were grown to OD600 = 0.8 in Terrific Broth plus antibiotics. Protein expression was induced for 4 hr at 37°C with 0.4 mM IPTG. Cells were harvested by centrifugation, flash frozen and stored at −80°C. Cell pellets were resuspended in cold lysis buffer (30 mM Tris pH 8.0, 600 mM KCl, 1 mM EDTA pH 8.0, 1 mM DTT, DNase, lysozyme, complete protease inhibitor cocktail and 0.2 mM PMSF), homogenized by douncing, and lysed by sonication (4 pulses of 30 s). Lysates were cleared for 30 min at 33,500 × g, and the supernatant was mixed with 0.5 mL glutathione-agarose beads (Thermo Fisher Scientific, Pittsburgh, PA), and incubated for 1 hr at 4°C. Beads were washed three times in 30 mM Tris pH 8.0, 600 mM KCl, 1 mM EDTA pH 8.0, and proteins were eluted in the same buffer plus 5% glycerol and 30 mM glutathione. Eluted proteins were mixed with 0.5 mL Ni-NTA-agarose beads in 30 mM Tris pH 8.0, 600 mM KCl, 1% Triton X-100, plus 30mM Imidazole, and incubated for 1 hr at 4°C. Beads were then washed three times in the same buffer lacking detergent, and fractions were eluted in the same buffer plus 300 mM Imidazole. Peak fractions were pooled, dialyzed overnight into HEKG5 buffer (20 mM HEPES, pH 7.5, 1mM EDTA, 150 mM KCl, and 5% glycerol), aliquoted, snap-frozen, and stored at −80°C. SNAP-tagged APC-B protein was purified in the same manner, except while still on the Ni-NTA-agarose beads it was labeled overnight at 4°C with 50 μM SNAP-Surface649 dye (NEB, Ipswich, MA). Beads were washed five times to remove excess dye, and proteins were eluted, dialyzed, aliquoted, and stored as above. Percent labeling of SNAP-APC-B and SNAP-APC-C was determined by measuring fluorophore absorbance using the extinction coefficient for SNAP-surface 649: ε655 = 250,000 M-1 cm-1. SNAP-APC-B and SNAP-APC-C labeling efficiency was 80%–86% for different batches. Concentrations of proteins were determined by band intensity on Coomassie-stained gels compared to a BSA standard curve using a BioRad Chemidoc MP imaging system, and quantified by densitometry using Imaging Lab version 6.0.0 software (Biorad).

Wild-type and mutant EB1 proteins were purified essentially as described [17], with minor modifications as follows. Briefly, plasmids expressing GST-EB1 proteins were transformed into fresh competent *E. coli* cells and grown in Terrific Broth under antibiotic selection. Induction tests showed that inducing expression with IPTG yielded insoluble proteins, and therefore, GST-EB1 was

Please cite this article in press as: Juanes et al., EB1 Directly Regulates APC-Mediated Actin Nucleation, Current Biology (2020), https://doi.org/10.1016/j.cub.2020.08.094

purified from cells without inducing expression, which yielded soluble proteins. Cells were harvested by centrifugation and stored at −80°C. Cell pellets were resuspended in cold lysis buffer (30 mM Tris pH 8.0, 150 mM KCl, 1 mM EDTA pH 8.0, 1 mM DTT, DNaseI, lysozyme, complete protease inhibitor cocktail and 0.2 mM PMSF), and lysed with lysozyme for 30 min, mixing occasionally by gentle inversion. Lysates were cleared for 15 min at 10,000 × g, and then cleared using a syringe filter (0.22 μm). Clarified lysates were slowly loaded on a GSTrap column (GE Healthcare) equilibrated in lysis buffer. After washing, Precision protease was added to the GSTrap column, and incubated overnight at 4oC to release untagged EB1. Released protein was eluted in lysis buffer, concentrated, and exchanged into HEKG10 buffer (20 mM HEPES, pH 7.5, 1mM EDTA, 150 mM KCl, and 10% glycerol) using a G-25 desalting column (GE Healthcare), then aliquoted, snap-frozen, and stored at −80°C. In some cases, purified EB1 was labeled on surface cysteines using Alexa Fluor 594 C5 Maleimide (Thermo Fisher Scientific). This was achieved by exchanging EB1 into HEKG10 with 10 mM TCEP and a 5 molar excess of dye, and incubating overnight at 4°C. Free dye was removed using a gravity G-25 desalting columns, and the protein was aliquoted, snap-frozen, and stored at −80°C. Percent labeling was determined by measuring fluorophore absorbance using the extinction coefficient for Alexa Fluor 594 C5 Maleimide: ε655 = 250,000 M-1 cm-1. EB1-594 labeling efficiency was 20%–26% for different batches.

Bulk assays

For pyrene-actin assembly assays, gel filtered monomeric actin (2 μM; 5% pyrene-labeled) in G-buffer (5 mM Tris-HCl pH 8.0, 0.2 mM ATP, 0.2 mM CaCl2, and 0.2 mM DTT) was converted to Mg-ATP-actin immediately before each reaction as described [62]. Actin was mixed with proteins or control buffer, then 3 μL of 20 × initiation mix (40 mM MgCl2, 10 mM ATP, 1 M KCl) was added to initiate polymerization. Fluorescence was monitored at excitation 365 nm and emission 407 nm at 25°C in a fluorimeter (Photon Technology International, Lawrenceville, NJ). For measuring G-actin binding by change in fluorescence, 100 nM Ca-ATP–G-actin (100% pyrene-labeled) was incubated for 60 min with 100 nM Latrunculin B in G-buffer. Then, 55 μL of this mixture was added to 5 μL APC-B and/or EB1 at different concentrations (0–1000 nM) in HEKG5 buffer, incubated for 60 min at room temperature to reach steady state, and then pyrene fluorescence was measured in a fluorimeter at 25°C using excitation 365 nm and emission 407 nm.

In vitro TIRF microscopy and single molecule binding assays

Glass coverslips (60 × 24 mm; Thermo Fisher Scientific) were cleaned by sonication for 30 min in detergent, followed by 1 M KOH, and 1 M HCl, and then stored in 100% ethanol. To biotin-anchor SNAP-APC proteins to the surface for single molecule binding assays, coverslips were first coated with a mixture of 4 mg/mL polyethylene glycol (PEG)-silane and 80 μg/mL biotin-PEG in 80% ethanol pH 1.0, then washed with water and dried with compressed N2. PEG-coated coverslips were stored for 1-3 days at 70°C prior to use. Flow chambers were constructed by sandwiching coverslips on top of plastic flow chambers (Ibidi, Fitchburg, WI) using double-sided tape (2.5 cm × 2 mm × 120 μm) and five-minute epoxy resin (Devcon, Riviera Beach, FL).

For each TIRF reaction, 4 μg/mL streptavidin in HEK buffer (20 mM HEPES pH 7.4, 1 mM EDTA, 50 mM KCl) was flowed into the chamber for 15 s using a syringe pump (Harvard Apparatus, Holliston, MA), followed by washing with HEK buffer + 1% BSA. The chamber was then equilibrated with TIRF buffer (10 mM HEPES pH 7.4, 50 mM KCl, 1 mM MgCl2, 1 mM EGTA, 0.2 mM ATP, 10 mM DTT, 15 mM glucose, 20 μg/mL catalase, 100 μg/mL glucose oxidase, 10 mM Imidazole, and 0.5% methylcellulose (4000 cP)). Where indicated, APC-B and EB1 proteins were diluted into TIRF buffer, and rapidly mixed with 1 μM actin monomers (10% OG-labeled, 0.2% biotinylated) and introduced into the flow. The flow cell was then immediately mounted on the microscope stage for imaging. The delay between mixing of proteins and initial imaging was 30 s. Time-lapse TIRF imaging was performed on a Ti200 inverted microscope (Nikon Instruments, New York, NY) equipped with 100 mW solid-state lasers (Agilent Technologies, Santa Clara, CA), a CFI Apo 60 × 1.49 N.A. oil-immersion TIRF objective (Nikon Instruments), a iXon EMCCD camera with a pixel size of 0.267 μm (Andor Technology), and an additional 1.5 × zoom module (Nikon Instruments). Focus was maintained using the Perfect Focus System (Nikon Instruments), and frames were captured every 5 s for a total of 600 s (10 ms at 488nm excitation, 10% laser power) using NIS Elements software (Nikon). Image analysis was performed in ImageJ. Background fluorescence was removed from each time series using the background subtraction tool in Fiji (rolling ball radius, 50 pixels). For measuring the number of actin filaments nucleated in TIRF reactions, fields of view were analyzed 300 s after the initiation of actin assembly.

For single molecule colocalization experiments, 25 pM SNAP-649-Biotin-APC-B (89% labeled), SNAP-649-Biotin-APC-C (60% labeled), or SNAP-649-Biotin-APC-B^{LRDP}molecules (84% labeled) was preincubated for 1 hr with 500 nM EB1-Alexa-594 (24% labeled) in TIRF buffer, then introduced into the flow chamber and imaged. Labeled APC proteins were anchored to the viewing surface, and then APC and bound EB1 molecules were imaged in separate channels. Images were collected at 100 ms exposures times for each channel and 10-20 images were collected per condition. Images analysis was performed using a custom written MATLAB (Natick, MA) code. Background fluorescence was subtracted from each image using a rolling average, and manual thresholding was used to generate a binary mask of each channel. Colocalization was defined as overlap of at least 3 pixels from each protein spot in each of the binary masks. The fraction of APC molecules with EB1 bound (colocalized spots) was determined. Only ~20% of the anchored labeled APC molecules were competent to bind EB1 (Figures 1G and 1H). This is a common observation in single molecule binding assays, as tethering to the surface can render a large fraction of anchored molecules incapable of binding to a specific ligand [63]. Fortunately, the 'inactive' fraction of APC molecules, which do not bind EB1, do not impact the binding behavior of the remaining, active APC molecules with EB1, and thus do not impact the analysis or the interpretation of the results. The specificity of binding between EB1 and APC (C-terminal third of protein) has been demonstrated in previous studies [1, 6]. As an additional control for non-specific interactions, we verified that EB1 binding to anchored APC molecules on the surface was reversible, i.e., EB1 molecules

Please cite this article in press as: Juanes et al., EB1 Directly Regulates APC-Mediated Actin Nucleation, Current Biology (2020), https://doi.org/10.1016/j.cub.2020.08.094

eventually dissociated from APC, and that this effect was not due to photobleaching. Additionally, we observed no colocalization between labeled EB1 and APC after the images of the two channels (EB1 and APC) were rotated by 90 degrees with respect to each other. Thus, colocalization does not arise from non-specific interactions of EB1 with the surface.

RNAi silencing and plasmid transfections

As mentioned above, human osteosarcoma (U2OS, HTB96) and human breast cancer (MDA-MB-231, HTB-26) cell lines were obtained from ATCC. Cell culture experiments, for both cell lines, were carried out in 6-well plates (MatTek Corporation, Ashland, MA), seeding each well with approximately 60,000 cells. Transfection efficiencies (for both U2OS and MDA-MB-231 cells) were optimized by carefully titrating the loads of oligos and plasmids, and testing different incubation times for key steps in the transfection protocol. This resulted in consistent transfection efficiencies of 75%–80% for plasmids, quantified by visualization of the plasmid-derived GFP signal, and 85%–99% for APC and EB1 knockdowns, quantified by visualizing uptake of a Cy5-labeled dye mixed with the knockdown oligos. To silence endogenous EB1, 8-12 hr after seeding, cells were transfected with 60 nM RNAi oligos using Lipofectamine RNAiMAX (Thermo Fisher Scientific), according to the manufacturer's instructions. RNAi oligos were directed against the 3′ UTR region of human EB1 (si-EB1): 5′-UUAAAUACUCUUAAGGCAUUU-3′ sense and 5′-AAAUGCCUUAAGAGUAUUUAA-3′ antisense [26] (Integrated DNA Technologies, Inc., Coralville, Iowa, USA). To silence endogenous APC, 8-12 hr after seeding, cells were transfected with 50 nM RNAi oligos using Lipofectamine 3000 (Thermo Fisher Scientific), according to the manufacturer's instructions. RNAi oligos were directed against the mRNA coding region of human APC (si-APC): 5′-GGAUCUGUAUCAAGCCGUUTT-3′ sense and 5′-AACGGCUUGAUACAGAUCCTT-3′ antisense [15] (Thermo Fisher Scientific). Cells were transfected in parallel with control 'scramble' RNAi oligos: 5′-CAGUCGCGUUUGCGACUGG-3′ with dTdT 3′ overhangs. For EB1 rescue experiments, 10-12 hr after silencing, cells were transfected with 200 ng of human EB1-GFP plasmid as in Juanes et al. [15], using Lipofectamine 3000. For EB1-GFP wild-type ($EB1^{WT}$) and mutants (OE-$EB1^{Q102E}$ or OE-$EB1^{K89E}$), and APC-m4 experiments, 10-12 hr after seeding cells, 1 μg of plasmid was introduced ectopically in cells, without depletion of endogenous EB1 or APC using Lipofectamine 3000 (Thermo Fisher Scientific). 24 hr after EB1 or APC plasmid transfection, the cells were collected for western blotting or replated for 6-8 hr prior to fixation and immunofluorescence.

Western blotting

Western blotting was used to determine endogenous EB1 and APC proteins levels after RNAi silencing, and ectopic EB1 and APC levels after rescue or overexpression of EB1 and ectopic expression of APC-m4 in U2OS and MDA-MB-231 cells. Cells were pelleted and resuspended in lysis buffer (150 mM NaCl, 1.0% NP-40, 1.0% sodium deoxycholate, 1% SDS, 50 mM Tris, pH 7.5, 2 mM EDTA, 0.2 mM sodium orthovanadate, 20 mM β-glycerophosphate, 50 mM sodium fluoride, 1 mM PMSF, 1 mM DTT, and 1 × Roche complete protease inhibitor mixture), and incubated at 4°C for 30 min with vortexing every 2 min. Lysates were precleared by centrifugation at 15,300 x g for 20 min at 4°C, and the soluble protein concentration was determined by Bradford assay (Biorad, Hercules, CA). Equal amounts of lysate (total protein) were compared on immunoblots. Blots were probed with 1:1000 mouse anti-EB1 (Clone 5/EB1 #610534; BD Transduction Laboratories), 1:500 rabbit anti-APC (ab154906; Abcam, Cambridge MA), 1:2000 rabbit anti-GFP (ab6556; Abcam), or 1:2000 rabbit/human anti-GADPH (ab9489; Abcam, Cambridge, MA). Blots were washed and probed with infrared dye–conjugated secondary antibodies (Rockland Immunochemicals, Pottstown, PA). Bands were detected using a BioRad Chemidoc MP imaging system, and quantified by densitometry using Imaging Lab version 6.0.0 software (Biorad). GADPH was used as loading control. For the quantitative western blots used to determine levels of endogenous EB1 and APC, known amounts of purified EB1 or APC-C (residues 2130-2843) were run on gels alongside U2OS cell lysates, blotted, and probed with anti-EB1 or anti-APC antibodies. Band densitometry as above was used to generate a standard curve for the purified proteins, and the amount of EB1 or APC protein in the cell lysates was determined by comparison to the standard curves. Values were averaged from three independent blots. For calculations of cellular concentrations of EB1 and APC, the concentration of total protein in the cytoplasm was assumed to be 100 mg/ml [36]. The amount (in grams) of EB1 and APC in 25 or 60 μg of lysate, respectively, was determined, and then the molar concentration of each protein was calculated based its known molecular weight and the considerations above.

Immunostaining of fixed cells

Transfected cells were replated for 16-18 hr on 3 × 1 × 1 mm glass coverslips (VWR International, Radnor, PA), which had been acid-washed and precoated with collagen I (Advanced BioMatrix, Carlsbad, CA). For imaging endogenously-expressed phospho-Paxillin (P-Pax) and/or overexpressed EB1-GFP (to validate transfection) along with F-actin, cells were fixed at room temperature for 15 min using 4% Formaldehyde methanol-free in 1 × PBS (2.7 mM KCl, 1.8 mM KH2PO4, 10 mM Na2HPO4, 140 mM NaCl pH 7.4), permeabilized for 10 min in 1 × PBS plus 0.5% Triton X-100 and 0.3 M glycine, and incubated for 1 hr at room temperature in a solution of 1% BSA dissolved in PBST (1 × PBS, 0.1% v/v Tween-20). For immunostaining, cells were incubated for 12 hr at 4°C with primary antibody 1:500 rabbit anti-phospho-Paxillin (Tyr118) (PP4501; ECM Biosciences). Next, coverslips were washed three times with 1 × PBST and incubated for 1 hr at room temperature with secondary antibody 1:1000 goat anti-rabbit Alexa Fluor-555 (A-21428, Thermo Fisher Scientific) along with 1:1000 Phalloidin-568 (A-12380, Thermo Fisher Scientific) to stain F-actin. Then coverslips were washed three times with 1 × PBS plus 0.1% Tween-20, once with PBS, and mounted with AquaMount (Thermo Fisher Scientific) before imaging. Cells were imaged on a Nikon i-E upright confocal microscope (Nikon Instruments) equipped with a CSU-W1 spinning disk head (Yokogawa, Tokyo, Japan), 100 mW solid-state lasers, an emission tuner for 561 nm wavelength, 60x oil objective (NA 1.4; Nikon Instruments), and an Ixon 897 Ultra-CCD camera (Andor Technology). Images were captured as stacks (9 planes, 0.5 μm steps,

Please cite this article in press as: Juanes et al., EB1 Directly Regulates APC-Mediated Actin Nucleation, Current Biology (2020), https://doi.org/10.1016/j.cub.2020.08.094

60%–80% laser power) with sequential 100-200 ms exposures at 561 nm using Nikon Elements software (version 4.30.02; Nikon Instruments).

For imaging endogenous alpha-actinin and alpha-tubulin, alongside F-actin, cells were fixed and permeabilized as above, and then incubated for 1 hr at room temperature with 1:100 mouse BM-75.2 alpha-actinin antibody (A5044, Sigma-Aldrich), or with 1:1000 mouse alpha-tubulin antibody (sc-32292; Santa Cruz Biotechnology). After washes with 1 × PBST, coverslips were incubated for 1 hr at room temperature with 1:1000 Phalloidin-568 (A-12380, Thermo Fisher Scientific) to stain F-actin, and either 1:1000 goat anti-mouse AlexaFluor-488 (A-32723) for alpha-actinin or 1:1000 goat anti-mouse AlexaFluor-633 (A-21050) for alpha-tubulin. Cells were imaged on a laser scanning confocal inverted Nikon Ti-E-PFS3 eclipse microscope (Nikon Instruments, New York, NY) equipped with 100 mW solid-state laser and emission tuner for 488, 561, 633 nm wavelengths, a 60x (NA 1.4) oil-immersion objective, a C2 imaging head (Nikon Instruments), and a 7-LED Light Engine array and a sCMOS camera (Andor Zyla) at room temperature. Images were acquired using Nikon Elements software (version 4.30.02) with 2 × averaging stacks (7 planes stacks, 0.5 μm steps) at 1% laser power, with 32 ms exposures for alpha-actinin and F-actin; and 17 ms exposures for tubulin and F-actin.

To control for the loss of labile actin structures in our cell staining, we performed separate experiments (Figures S2B and S2C) using a different fixation method optimized for preserving the actin cytoskeleton [22]. Cells were fixed on coverslips with pre-warmed 4% formaldehyde methanol-free in 1 × PBS (2.7 mM KCl, 1.8 mM KH2PO4, 10 mM Na2HPO4, 140 mM NaCl pH 7.4) and 0.25% glutaraldehyde for 20 min. This combination of fixatives increases the degree of crosslinking. Coverslips were then washed three times with warm 1 × PBS, permeabilized for 1 min using 1 × PBS plus 0.1% Triton X-100, washed three times with room temperature 1 × PBS, incubated for 1 hr at room temperature with 1:200 Phalloidin-568 (A-12380, Thermo Fisher Scientific), and finally washed three times with room temperature 1 × PBS. Cells were imaged as above on the laser scanning confocal inverted Nikon Ti-E-PFS3 eclipse microscope (Nikon Instruments, New York, NY) except using a 100x (NA 1.45) oil-immersion objective. Images were acquired using Nikon Elements software (version 4.30.02) with 2 × averaging stacks (7 planes stacks, 0.5 μm steps) at 1% laser power with a 32 ms exposure.

Fiji was used to generate maximum intensity projections from all images. For each cell, the raw cellular fluorescence intensity and cell area, calculated using Fiji, was used to determine F-actin and alpha-actinin densities (fluorescence intensity divided by cell area). To quantify microtubule density at the leading edge, a box (15 × 15 μm2) was positioned at the cell edge, extending back toward the center of the cell, and mean fluorescence intensity was measured in the box using Fiji and shown per μm2. To quantify F-actin density at individual focal adhesions, the ratio of the integrated fluorescence intensity of F-actin versus Phospho-Paxillin (P-Pax) at each focal adhesion was quantified in an automated fashion using a custom script in MATLAB.

Wound healing and chemotaxis assays

For would healing assays, U2OS cells (1 × 106) were plated on 6-well dishes, then cells were transfected with siRNA oligos and/or plasmids as described. After 24 hr, cells were replated onto μ-dishes 35 mm containing a sterile silicone 2 well culture-insert (Ibidi, Martinsried, Germany) that patterns cells around an open gap. After cells grew to confluency (24 hr), the silicone insert was removed, creating a gap (wound), into which cells migrated. The dishes were replenished with DMEM media containing high glucose buffer (GIBCO, Life Technologies), 10% FBS, 20 mM L-glutamine, and 1 mM sodium pyruvate. Wound closure was monitored at 10 min intervals for 16 hr, maintaining cells at 37°C with 5% CO2 using an Okolab controller adapted to the inverted Nikon Ti-E-PFS3 eclipse microscope described above. Images were captured using a 10x (NA 0.3) air objective with a pixel size of 0.65 μm, and a Neo/Zyla sCMOS camera (Andor Technology, Neo/Zyla sCMOS camera Melville, NY) using NIS element analysis software (version 4.20, Nikon). Wound size and speed of wound closure were calculated using Wound Healing Automated Cellular Analysis System (ACAS) web-based quantitative image analysis from MetaVi Labs/Ibidi (https://www.metavilabs.com/; Cat# 32000-250). Data were combined from time-lapse image series collected from at least three independent experiments. Individual cells migrating at the edge of the wound were tracked, and their trajectories were obtained using the Chemotaxis and Migration Tool version 2.0 software (Ibidi, Germany).

For chemotaxis assays, MDA-MB-231 cells were grown on 6-well plates, then transfected with siRNA oligos and/or plasmids as described. To make cells responsive to the chemotractant gradient, the DMEM medium was replaced by serum-free growth medium UltraCULTURE TM (UC; Lonza) 24 hr after transfection. Then, adaptation was achieved in stepwise fashion, by replacing 20% of the serum-containing base medium with serum-free medium each of three times. Next, the adapted cells were replated on a Collagen-IV Chemotaxis μ-slide (Ibidi) according to manufacturer's protocol, and kept at 37°C with 5% CO2. A chemotactic gradient of FBS was established by placing media containing 0% FBS in the left reservoir, and media containing 10% FBS in the right reservoir of the middle chamber containing the cells. The assay was repeated independently at least two times using different chambers. Cells were maintained at 37°C on an Ibidi heated stage, and migration was monitored at 2 min intervals for 10 hr using the inverted Nikon Ti-E-PFS3 eclipse microscope described above. Images were captured using a 10x (NA 0.3) air objective with a pixel size of 0.65 μm, and a Neo/Zyla sCMOS camera (Andor Technology) using NIS element analysis software (version 4.20, Nikon). For each condition, at least 900 individual cells were tracked using FastTrack Artificial Intelligence (AI) automated analysis system, an artificial intelligence-based vision system from MetaVi Labs/Ibidi (Cat# 32200-3). The AI analysis system was iteratively trained to achieve accurate tracking for 100% of the cells in these experiments. All trajectories from cells moving at least 50 μm in 8 hr were analyzed. Data were combined from time-lapse image series collected from three independent experiments per condition. Parameters such as

Please cite this article in press as: Juanes et al., EB1 Directly Regulates APC-Mediated Actin Nucleation, Current Biology (2020), https://doi.org/10.1016/j.cub.2020.08.094

velocity, directionality index, and Euclidean distance accumulated (indicative of how straight cells move), were extracted from the track data. Trajectories were graphed as Rose plots using the Chemotaxis and Migration Tool version 2.0 software (Ibidi, Germany). Statistical analysis was performed with GraphPad Prism 6.0.

QUANTIFICATION AND STATISTICAL ANALYSIS

All experiments were repeated multiple times, as indicated in the figure legends. In each case, the data were pooled, averaged, and SD or SEM was calculated using GraphPad Prism (version 6.0c; GraphPad Software, La Jolla, CA). Figure legends specify the n and the error bars (SD or SEM) for each experiment. Data distributions were tested for normality using D'Agostino-Pearson omnibus normality test, and statistical significance of differences among conditions were calculated using ordinary one-way ANOVA Holm-Sidak's multiple comparisons tests in Prism software version 6.0c (GraphPad Software, La Jolla, CA). Differences were considered significant if P value < 0.05 (*), < 0.01(**), < 0.001(***), or < 0.0001 (****), as indicated in each figure legend.